SUPPORTING INFORMATION

High-Performance Hydrogen Evolution Electrocatalysis Using Proton-Intercalated TiO₂ Nanotube Arrays as Interactive Supports for Ir Nanoparticles

Uroš Lačnjevac,*[a] Rastko Vasilić,[b] Ana Dobrota,[c] Slađana Đurđić,[d] Ondřej Tomanec,[e] Radek Zbořil,[e] Shiva Mohajernia,[f] Nhat Truong Nguyen,[g] Natalia Skorodumova,[hi] Dragan Manojlović,[d] Nevenka Elezović,[a] Igor Pašti[ch] and Patrik Schmuki*[ef]

[a] Institute for Multidisciplinary Research, University of Belgrade, Kneza Višeslava 1, 11030 Belgrade, Serbia

[b] Faculty of Physics, University of Belgrade, Studentski trg 12-16, 11000 Belgrade, Serbia

[c] Faculty of Physical Chemistry, University of Belgrade, Studentski trg 12-16, 11000 Belgrade, Serbia

[d] Faculty of Chemistry, University of Belgrade, Studentski trg 12-16, 11000 Belgrade, Serbia

[e] Regional Centre of Advanced Technologies and Materials, Šlechtitelů 27, 78371 Olomouc, Czech Republic

[f] Department of Materials Science, WW4-LKO, University of Erlangen-Nuremberg, Martensstrasse 7, D-91058 Erlangen, Germany

[g] Department of Chemistry, University of Toronto, 80 Saint George Street, Toronto, ON, M5S 3H6, Canada

[h] Department of Materials Science and Engineering, School of Industrial Engineering and Management, KTH–Royal Institute of Technology, Brinellvägen 23, 100 44 Stockholm, Sweden

[i] Department of Physics and Astronomy, Uppsala University, Box 516, 751 20 Uppsala, Sweden

* Corresponding authors. E-mail addresses: uros.lacnjevac@imsi.bg.ac.rs (U. Lačnjevac), schmuki@ww.uni-erlangen.de (P. Schmuki).

EXPERIMENTAL

Materials and chemicals

Technical quality titanium sheets were cut into Ti disks (diameter 13.5 mm and thickness 2 mm) for anodization. Ammonium fluoride (≥ 98%, puriss. p.a.), perchloric acid (70.0-72.0%, puriss. p.a.) and Nafion® perfluorinated ion-exchange resin (5 wt% solution in lower aliphatic alcohols/H_2O mix) were purchased from Sigma-Aldrich, hydrochloric acid (35% g.r.) and sulfuric acid (96% g.r.) from Lach-Ner, ethanol (94-96%) and Pt/C (nominally 40 wt% Pt on carbon black HiSPEC® 4000) from Alfa Aesar, while all other chemicals and materials were purchased from different manufacturers: ethylene glycol (≥ 99.5%, puriss. p.a., Fluka Analytical), acetone (≥ 99.5%, p.a., Chem-Lab), nitric acid (65%, Macron Fine Chemicals), iridium(III) chloride hydrate ($IrCl_3 \cdot xH_2O$, Ir content > 53.0%, Merck) and Ir/C (10 wt% Ir on Vulcan, PK Catalyst). Extra pure UV water (18.2 MΩ cm, Smart2PureUV, TKA) was used for all experimental procedures.

Synthesis of Ir@TNT

Ti disks were polished with 320, 500 and 1200 grit SiC abrasive papers, cleaned ultrasonically for 5 min in acetone and 5 min in ethanol, and dried at 50 °C in air. TNT coating layers were prepared through a one-step anodization procedure. A Ti disk was mounted into a cylinder-like polytetrafluoroethylene (PTFE) holder with an Au plate back contact and a top removable lid having a 10.5 mm opening that allowed only a disk surface area of 0.87 cm^2 to be exposed to the solution. Anodization was performed by means of a PEQLAB 55-EV231 electrophoresis power supply in a 250 mL homemade glass beaker cell in a two-electrode configuration with a platinized Ti mesh cathode positioned at 3 cm from the Ti disk surface. A conventional ethylene

glycol solution containing 0.30 wt% NH_4F and 1.0 wt% H_2O was used for all anodizations. The cell voltage was first ramped up from 0 V to 60 V at a sweep rate of 15 V min^{-1} and then kept at 60 V for 80 minutes (TNT arrays denoted by **TNT-80**). Anodization conditions were varied to produce TNT arrays with two distinctive top surface microstructures: **open-top** and **nanograss**. For achieving the open-top TNT arrays, the solution was magnetically stirred at moderate intensity and maintained at a temperature of 24-25 °C, whereas the nanograss TNT arrays were obtained by applying higher rotating rates of the magnetic stir bar and elevated temperatures (29-30 °C). Specifically, the stirrer dial of the magnetic stirrer (T.ARE, Velp Scientifica) was set to rotational speed "2" for obtaining open-top nanotubes and speed "4" for nanograss nanotubes. For comparison purposes, one TNT sample was anodized by imposing the nanograss conditions at 60 V for only 25 minutes (denoted by **TNT-25**). Ti disks with as-formed TNTs (denoted by **as-TNT**) were immediately immersed in acetone for 15 min, ultrasonicated for 30 s, rinsed with acetone and dried in air at 50 °C. Afterwards, as-TNT samples were annealed in air at 450 °C for 2.5 hours (**ann-TNT**) and then electrochemically hydrogenated/reduced by applying a constant cathodic current density of –23 mA cm^{-2} in 1.0 M $HClO_4$ for 30 minutes (**H-TNT**). Deposition of Ir nanoparticles on the walls of H-TNT arrays was carried out by a galvanic displacement method. H-TNT samples were kept submerged for 60 hours in aqueous solutions containing different concentrations of $IrCl_3$: **8**, **2**, **0.8**, **0.2** and **0.08 mM** (Fig. S1). In all the galvanic displacement solutions the total concentration of Cl^- ions was adjusted to 64 mM by adding an appropriate volume of 35% HCl. The composites obtained at different $IrCl_3$ concentrations are referred to as **Ir(*x* mM)@TNT**, where *x* indicates the Ir concentration applied. For easier comprehension, a unique color code has been consistently used for each sample throughout the manuscript.

Materials characterization

To identify the phase structure of TNT-based samples, X-ray powder diffraction (XRD) patterns were recorded using a Rigaku Ultima IV diffractometer equipped with Ni-filtered Cu Kα radiation (λ = 1.54178 Å) in Bragg-Brentano geometry over the 2ϑ range from 20° to 90° at an acquisition rate of 1° min^{-1} in 0.02° increments. The composition and surface chemical species were analyzed by X-ray photoelectron spectroscopy (XPS, PHI 5600, USA) and time-of-flight secondary ion mass spectrometry (ToF-SIMS, TOF.SIMS 5 spectrometer, IONTOF, Münster, Germany). XPS data were acquired by employing monochromatized Al Kα radiation and the binding energies of the core levels were calibrated by setting the Ti 2p peak at 458.5 eV. ToF-SIMS measurements were performed using a 25 keV Bi^{+} ion beam bunched down to < 0.8 ns. The primary ion dose density for spectra acquisition was 5×10^{11} ions cm^{-2} with an area of 100 μm × 100 μm, using negative polarity. Spectra were normalized to their total intensity and calibrated on C^{-}, O^{-}, C_2^{-}, C_2H^{-}, and C_3^{-}. Depth profiles were carried out in a dual beam approach with a crater size of 250 μm × 250 μm and a measured spot of 50 μm × 50 μm in the center of the crater. The sputter beam used was Cs (2 kV) and the measurement beam was Bi^{+}. The morphology was characterized using a field emission scanning electron microscope (FESEM, Hitachi S4800, Japan) operating at an accelerating voltage of 10 kV. For the cross-sectional characterization, two scalpel scratches were made across the top surface of TNT film modified Ti disks to produce a sufficient number of TNT layer parts with suitably exposed cross-section surfaces. The fine structural characterizations were conducted by means of a high resolution scanning transmission electron microscope (S/TEM, FEI Titan G2 60-300) equipped with high-angle

annular dark field (HAADF), energy dispersive X-ray spectroscopy (EDS) and electron energy loss spectroscopy (EELS) detectors for elemental mapping and chemical states analysis. For the TEM measurements, TNT layers were scratched off of the Ti disk, sprinkled with ethanol and applied on a holey carbon film-coated Cu TEM grid without any ultrasonication pretreatment in order to preserve as many whole tubes as possible. Inductively coupled plasma quadrupole mass spectrometry (ICP-QMS, iCAP Q, Thermo Scientific X series 2) was used to determine the Ir loading in the composites. A 50 mL beaker containing an Ir@TNT film modified Ti disk immersed in about 25 mL of aqua regia (a mixture of 35% HCl and 65% HNO_3 in a volume ratio of 4:1) was placed on a hot plate (250 °C), covered with a watch glass and heated for 6 hours with intensive boiling and occasional refilling of aqua regia to completely dissolve Ir. The Ti disk was then removed from the remaining solution (about 10 mL), 13 mL of 96% H_2SO_4 was added and the newly formed acid solution was allowed to evaporate while magnetically stirred for 2 hours on the hot plate heated at 250 °C in order to dissolve the TNT membrane that had detached from the Ti disk during the previous aqua regia treatment. 4 mL of the final solution (evaporated to about 10 mL) was transferred to a vial for the determination of Ir by ICP-QMS.

Electrochemical measurements

All electrochemical measurements were performed using a Gamry Interface 1000 potentiostat in a three-electrode setup. The working electrode was a TNT or Ir@TNT layer-coated Ti disk that was mounted into the cylindrical PTFE holder exposing a disk surface area of 0.87 cm^2. A Pt plate (dimensions: 1 cm × 1 cm) sealed in epoxy resin and a reversible hydrogen electrode (RHE) served as the counter and reference electrode, respectively, except in certain control experiments when a glassy carbon disk with a diameter of 14 mm was used as the counter

electrode. The electrolyte was a 1.0 M $HClO_4$ aqueous solution saturated with hydrogen, which was achieved by a continuous feed of 99.999 vol% purity H_2 gas, while the 250 mL beaker cell (the same one that was used for anodization procedures) was tightly covered with a PTFE lid to establish a hydrogen atmosphere above the solution. The RHE was connected to the cell through a Luggin capillary which was positioned at about 7 mm from the surface of the working electrode. The cell was placed in an aluminum Faraday cage and all experiments were carried out at room temperature (23 ± 1 °C) in the dark. All potentials given in the text are expressed against the RHE.

Cyclic voltammetry (CV) measurements for investigation of the electrochemical behavior of Ir@TNT composite electrodes were performed between 0.025 V and 1.2 V at a sweep rate of 100 mV s^{-1}. The interface capacitance was estimated from CV curves recorded between 0.8 V and 1.2 V at various sweep rates in the range from 10 to 1000 mV s^{-1}. To assess the catalytic activity, linear sweep voltammetry (LSV) measurements were carried out at a sweep rate of 1 mV s^{-1} in the anodic direction up to a potential of 0.1 V, while LSV curves recorded in the cathodic direction starting from 0.1 V were used to construct Tafel plots, since they provided more pronounced linearity of the Tafel slope regions. The current interrupt technique was applied to compensate all LSV curves for the ohmic potential drop in the solution. Potentiostatic electrochemical impedance spectroscopy (EIS) data were consecutively acquired in the direction of increasing HER overpotential by sampling 15-20 points per decade in the range of frequencies from 5 kHz to 30 mHz with an AC perturbation of 5 mV RMS. The EIS curves were fitted to appropriate models by a complex nonlinear least-squares technique using Gamry Echem Analyst software, version 6.25. All model parameters are normalized with respect to the geometric

surface area of the working electrode. Impedance measurements for Mott-Schottky analysis were conducted over a potential range from 1.5 V to 0.05 V in 50 mV increments using an AC amplitude of 5 mV RMS in the frequency range from 100 kHz to 1 Hz with 10 points per decade. Cycling stability tests were performed by sweeping the potential between 0.3 V and −0.065 V (or −0.100 V) for 1000 cycles at a rate of 100 mV s^{-1}. A long-term chronopotentiometric test was carried out at a current density of −25 mA cm^{-2} without IR compensation.

Benchmark **(Pt/C)@Ti disk** and **(Ir/C)@Ti disk** electrodes were prepared by a drop-cast method. Nominally, 1.0 mg of Pt(40 wt%)/C or 0.84 mg of Ir(10 wt%)/C powder was added to 1.0 ml of H_2O and ultrasonically dispersed for 50 minutes. Afterwards, to the suspension was added 20 µL of Nafion® solution and the mixture was kept under ultrasonic agitation for another 20 minutes. 60 µL of the final ink was dropped onto a Ti disk and spread over the surface area of 0.87 cm^2 (diameter 10.5 mm) which was identical to that of Ir@TNT samples. The Pt and Ir loadings in the **(Pt/C)@Ti disk** and **(Ir/C)@Ti disk** electrodes were 27 µg$_{Pt}$ cm^{-2} and 5.7 µg$_{Ir}$ cm^{-2}. The Ti disk with the drop-casted Pt/C or Ir/C was dried at 60 °C in air for 120 minutes, left overnight and then subjected to electrochemical measurements.

Computational methods

Since the catalyst support in this work has a rather complex morphology, for the purpose of a first-principles study we had to restrict the model to the size appropriate for such an approach. We modeled Ir deposition on the hydrogenated 001 surface of anatase TiO_2 with surface oxygen vacancies (as discussed in greater detail in the main text). All the calculations were based on spin-unrestricted density functional theory (DFT) calculations, using the Perdew-Burke-

Ernzerhof generalized gradient approximation (PBE-GGA) [E1] and the pseudopotential plane wave approach, as implemented in the Quantum ESPRESSO package [E2,E3]. Ultrasoft pseudopotentials were used and the plane wave basis set was expanded using a kinetic energy cutoff of 30 Ry and a charge density cutoff of 480 Ry. The first irreducible Brillouin zone was sampled using the 2×2×1 k-point set with Monkhorst–Pack sampling [E4].

The optimized lattice parameters of bulk anatase TiO_2 were found to be a = 3.816 Å and c = 9.513 Å, in agreement with experimental values (3.789 Å and 9.537 Å [E5], respectively). The pristine anatase TiO_2 (001) surface was modeled using a stoichiometric (3×3) supercell (96 atoms), with four layers of Ti and 8 layers of O. To remove the interactions of periodic images along the z-axis of the supercell, slabs were separated with 15 Å vacuum. Moreover, dipole correction was added to de-couple periodic images. During the relaxations, the bottom two Ti layers and the corresponding O layers were fixed at their bulk positions, while other atoms were relaxed until forces dropped below 0.010 eV Å^{-1}. Further discussion of surface models is provided in the Results & Discussion section.

In order to quantify the interactions of Ir with the TiO_2 surface and also the interactions of hydrogen with Ir@TiO_2 models, we use Ir and H adsorption energies (E_{ads}). The adsorption energy of Ir is calculated as integral adsorption energy:

$E_{ads}(Ir) = (E(Ir_n@TiO_2) - E(TiO_2) - nE(Ir))/n$

In the equation above, $Ir_n@TiO_2$, $E(TiO_2)$, and $E(Ir)$ are the total energy of the $Ir_n@TiO_2$ system, the total energy of the TiO_2 model surface and the total energy of an isolated Ir atom. For the adsorption energies of H similar equations apply, but the final system is $Ir_n@TiO_2$ with a certain

number of H atoms, while the adsorption energies refer either to an isolated H atom (E_{ads}(H)) or to 1/2 of the H_2 molecule in gas phase (E_{ads}(1/2H_2)).

To assess and compare the HER activity of different Ir$_n$@TiO$_2$ models, we calculated the Gibbs free energy for hydrogen adsorption from the following equation:

$$\Delta G_{ads}(\text{H}) = E_{ads}(1/2\text{H}_2) + \Delta E_{ZPE} - T\Delta S(\text{H})$$

where ΔE_{ZPE} is the difference in zero-point energy between the adsorbed hydrogen and hydrogen in the gas phase, T is temperature and ΔS(H) is the entropy difference between the adsorbed state and the gas phase. Following Ref. [E6], ΔG_{ads}(H) is obtained by adding +0.24 eV to E_{ads}(1/2H_2).

References

[E1] J. P. Perdew, K. Burke and M. Ernzerhof, *Phys. Rev. Lett.*, 1996, **77**, 3865–3868.

[E2] P. Giannozzi, S. Baroni, N. Bonini, M. Calandra, R. Car, C. Cavazzoni, D. Ceresoli, G. L. Chiarotti, M. Cococcioni, I. Dabo, A. Dal Corso, S. de Gironcoli, S. Fabris, G. Fratesi, R. Gebauer, U. Gerstmann, C. Gougoussis, A. Kokalj, M. Lazzeri, L. Martin-Samos, N. Marzari, F. Mauri, R. Mazzarello, S. Paolini, A. Pasquarello, L. Paulatto, C. Sbraccia, S. Scandolo, G. Sclauzero, A. P. Seitsonen, A. Smogunov, P. Umari and R. M. Wentzcovitch, *J. Phys.: Condens. Matter*, 2009, **21**, 395502.

[E3] P. Giannozzi, O. Andreussi, T. Brumme, O. Bunau, M. Buongiorno Nardelli, M. Calandra, R. Car, C. Cavazzoni, D. Ceresoli, M. Cococcioni, N. Colonna, I. Carnimeo, A. Dal Corso, S. de Gironcoli, P. Delugas, R. A. DiStasio Jr, A. Ferretti, A. Floris, G. Fratesi, G. Fugallo, R. Gebauer, U. Gerstmann, F. Giustino, T. Gorni, J. Jia, M. Kawamura, H.-Y. Ko, A. Kokalj, E. Küçükbenli, M. Lazzeri, M. Marsili, N. Marzari, F. Mauri, N. L. Nguyen, H.-V. Nguyen, A. Otero-de-la-Roza, L. Paulatto, S. Poncé, D. Rocca, R. Sabatini, B. Santra, M. Schlipf, A. P. Seitsonen, A. Smogunov, I. Timrov, T. Thonhauser, P. Umari, N. Vast, X. Wu and S. Baroni, *J. Phys.: Condens. Matter*, 2017, **29**, 465901.

[E4] H. J. Monkhorst and J. D. Pack, *Phys. Rev. B*, 1976, **13**, 5188–5192.

[E5] M. Horn, C. F. Schwerdtfeger and E. P. Meagher, *Z. Kristallogr. Kristallgeom. Kristallphys. Kristallchem.*, 1972, **136**, 273–281.

[E6] J. K. Nørskov, T. Bligaard, A. Logadottir, J. R. Kitchin, J. G. Chen, S. Pandelov and U. Stimming, J. Electrochem. Soc., 2005, 152, J23–J26.
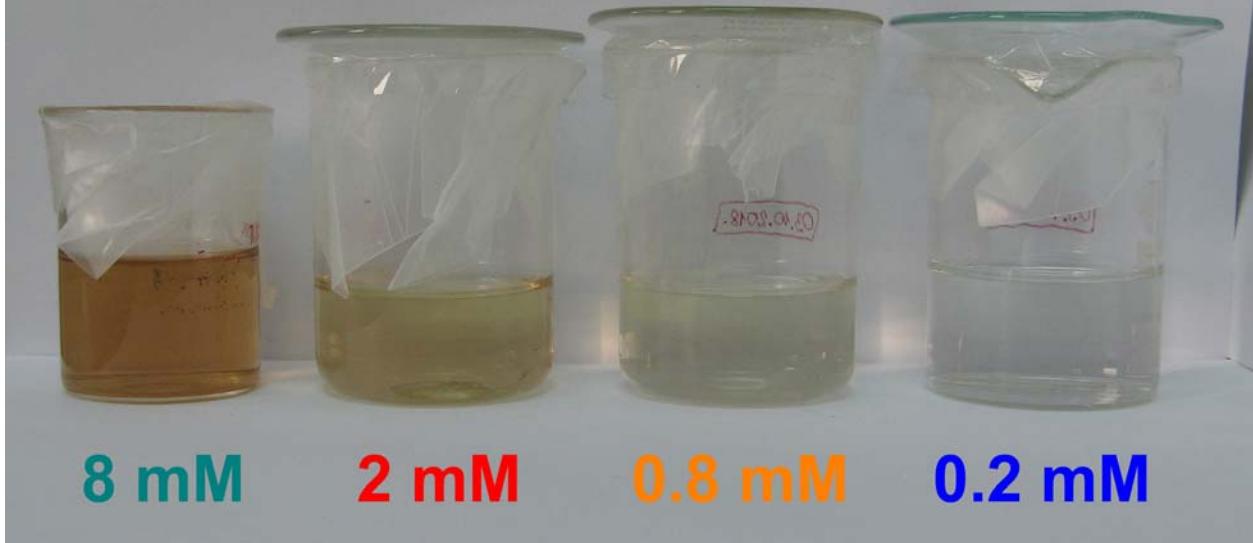
**Fig. S1.** Digital photograph of galvanic displacement solutions containing different concentrations of IrCl₃ (marked in the figure).
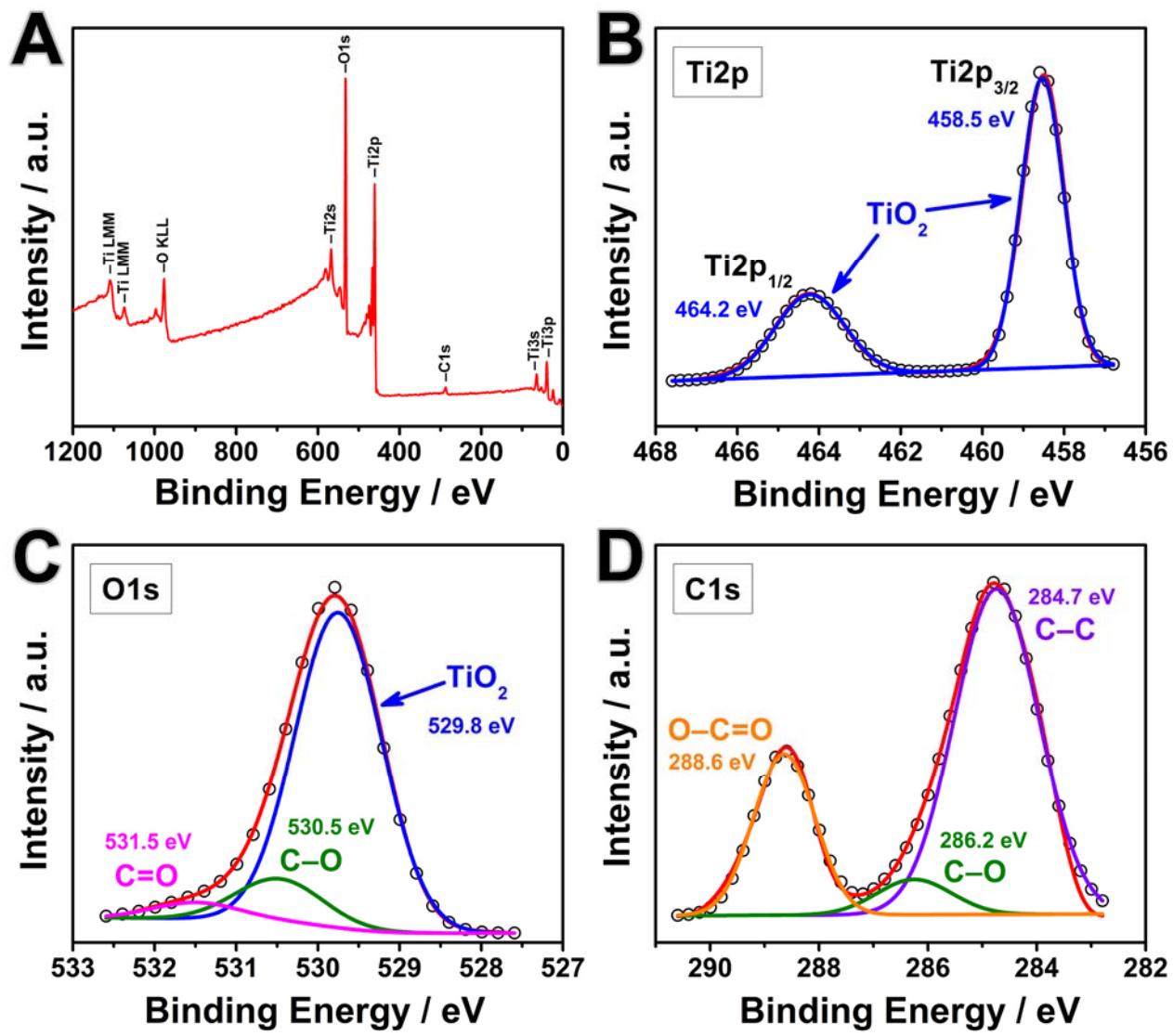
Fig. S2. XPS analysis of **Ir(0.2 mM)@TNT-80**: (A) survey, and high-resolution (B) Ti 2p, (C) O 1s and (D) C 1s spectra.
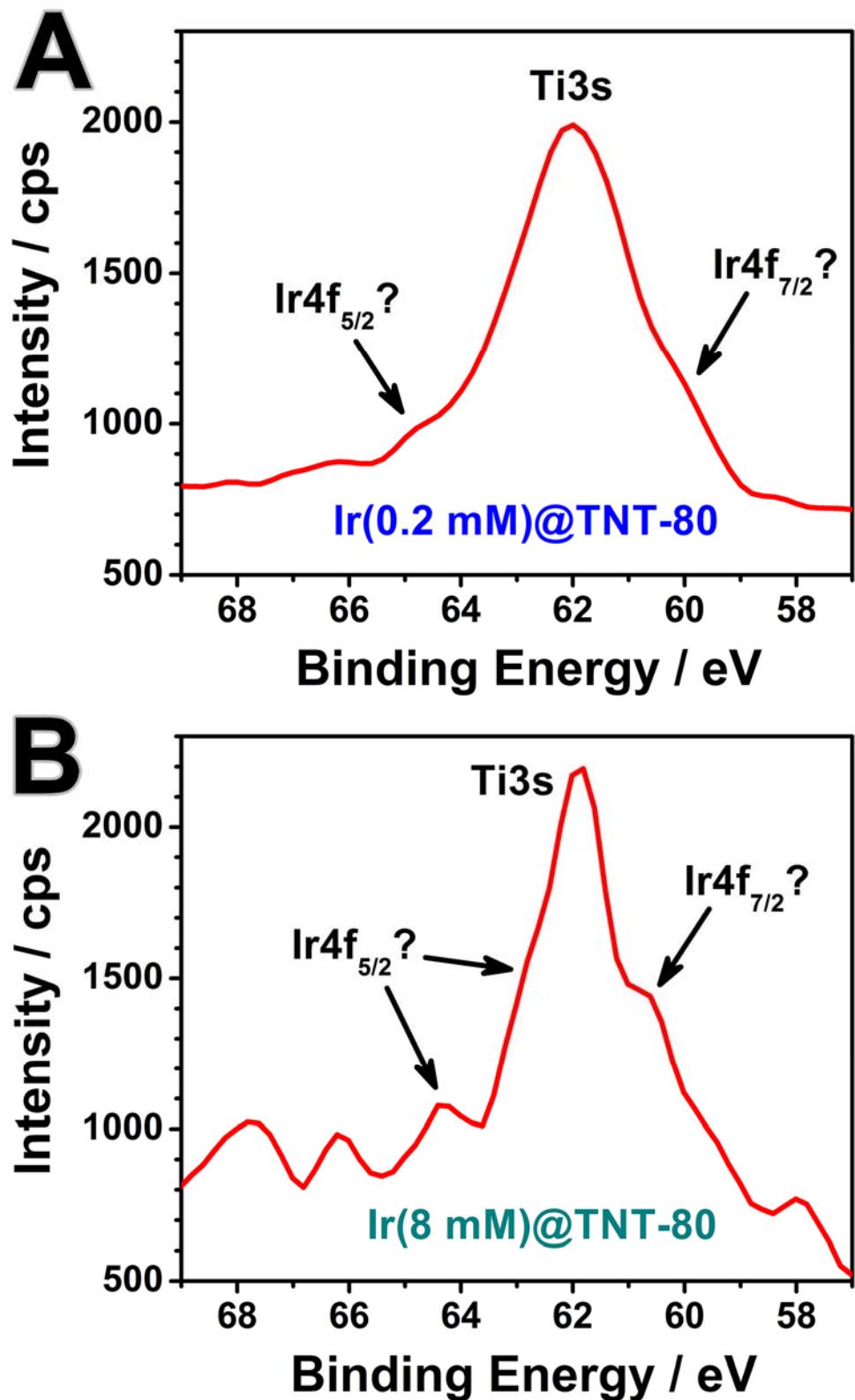
Fig. S3. High-resolution XP spectra of (A) **Ir(0.2 mM)@TNT-80** and (B) **Ir(8 mM)@TNT-80** recorded in the Ti 3s + Ir 4f region.
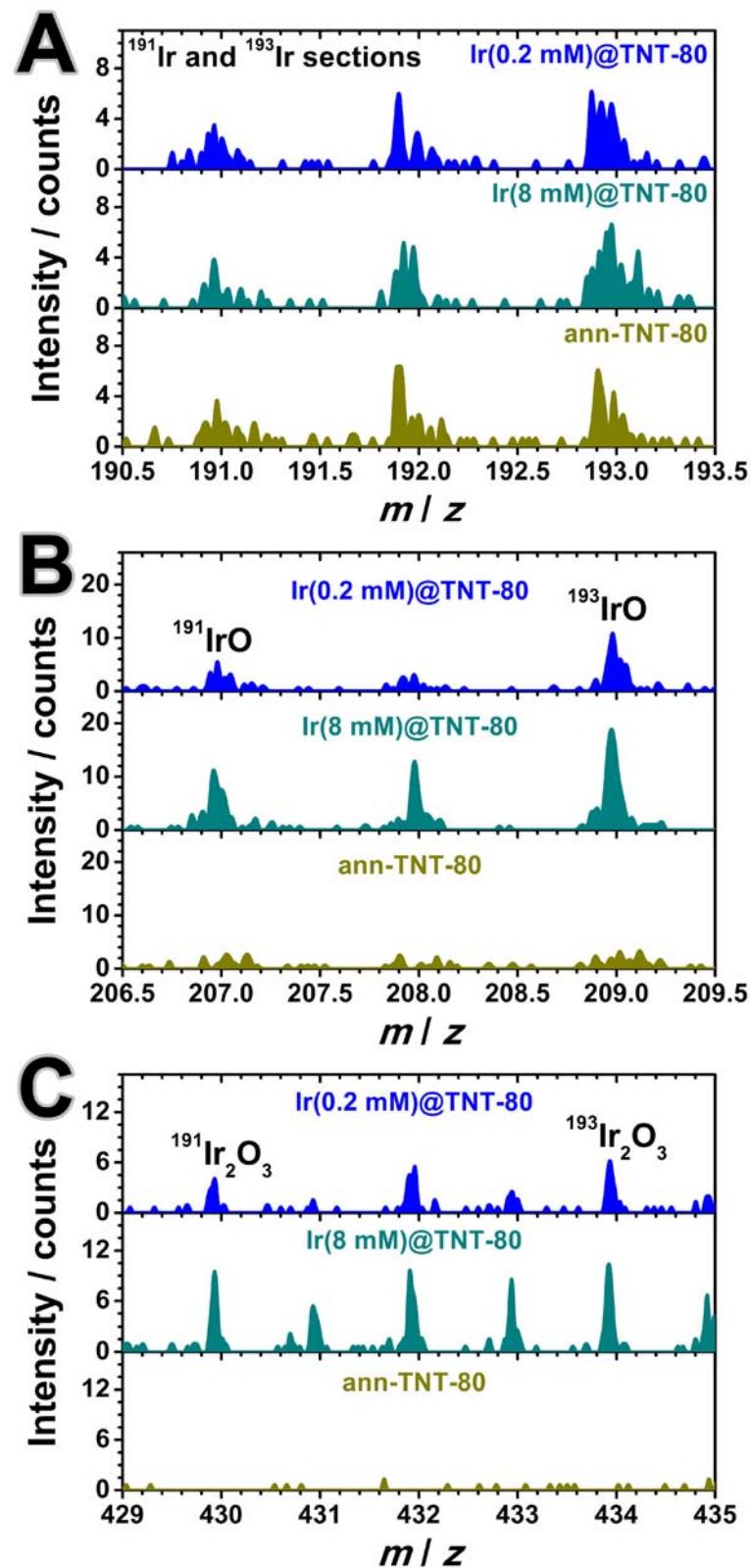
Fig. S4. ToF-SIM spectra recorded at the top surface of **Ir(0.2 mM)@TNT-80**, **Ir(8 mM)@TNT-80** and **ann-TNT-80**: (A) elemental Ir, (B) IrO and (C) Ir_2O_3 sections.
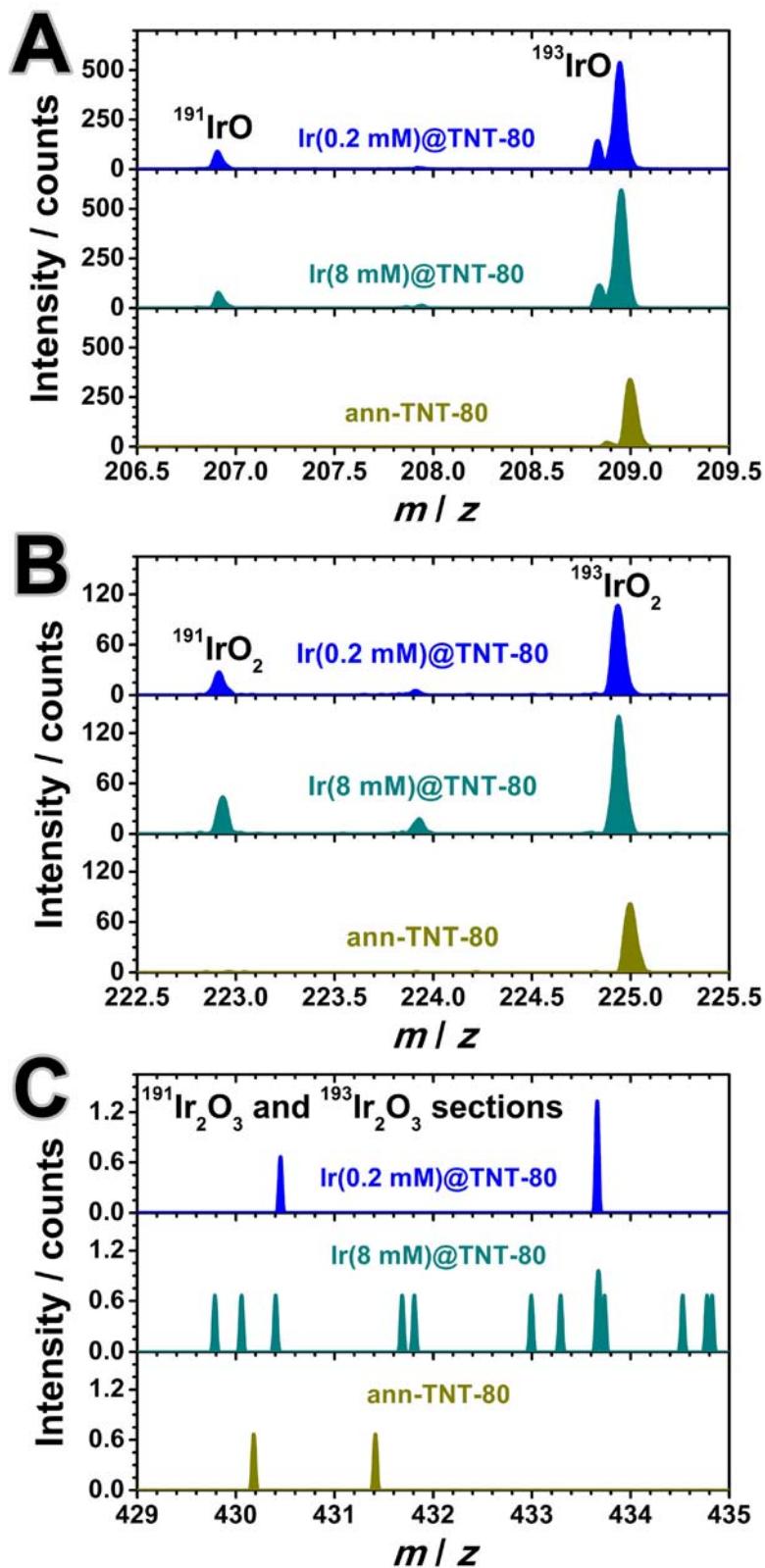
Fig. S5. ToF-SIM spectra recorded at a depth of ~300 nm for **Ir(0.2 mM)@TNT-80**, **Ir(8 mM)@TNT-80** and **ann-TNT-80**: (A) IrO, (B) IrO_2 and (C) Ir_2O_3 sections.
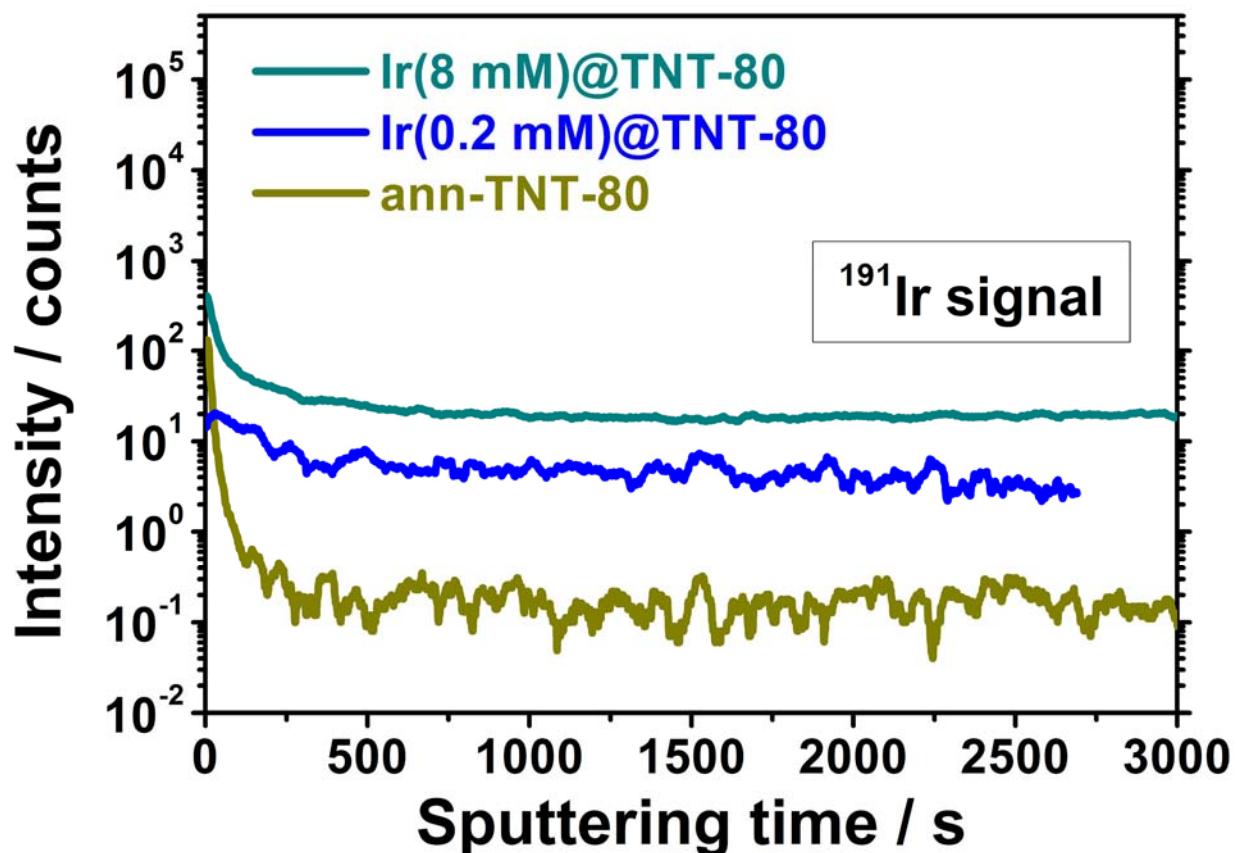
Fig. S6. ToF-SIMS depth profiles of [191]Ir for **Ir(8 mM)@TNT-80**, **Ir(0.2 mM)@TNT-80** and **ann-TNT-80** (final depth ~1.5 μm).
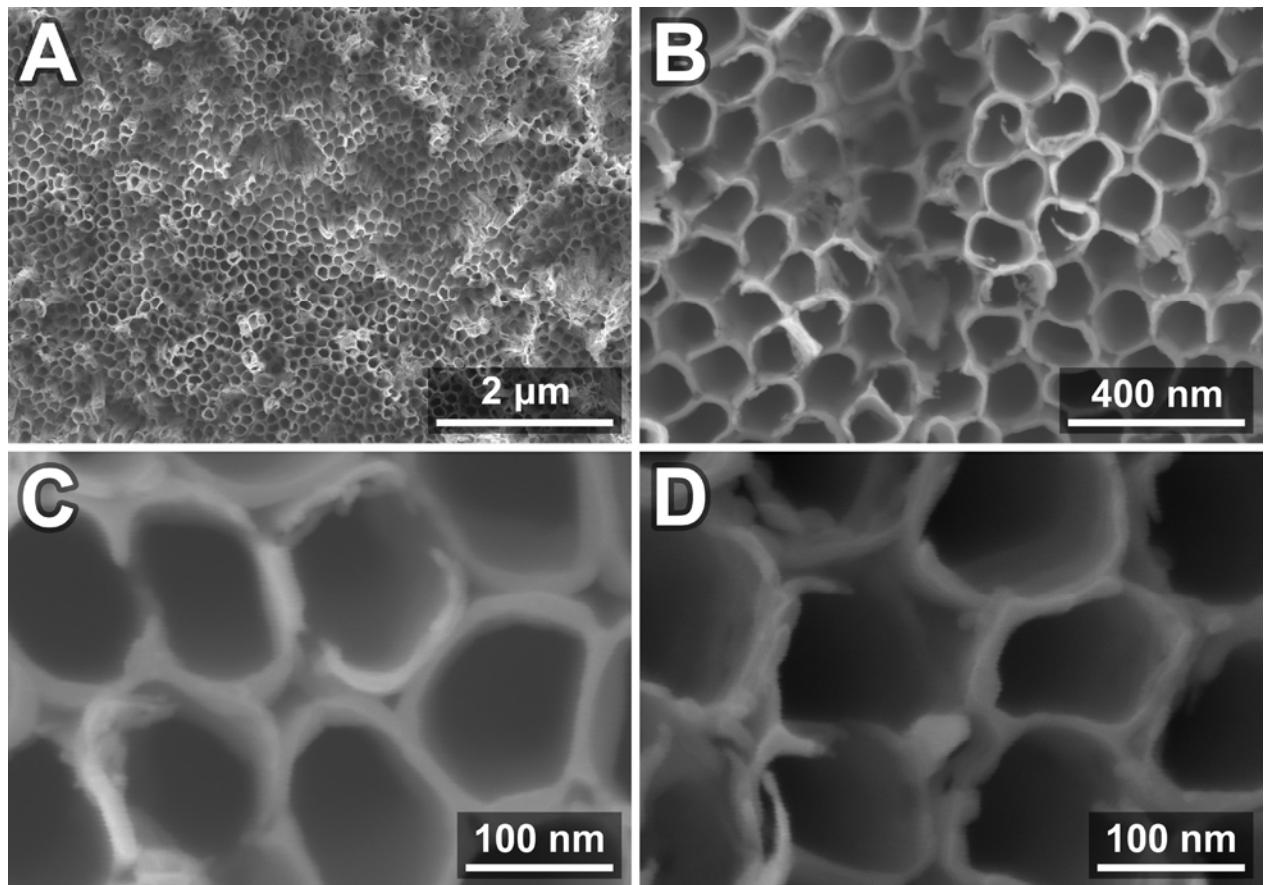
Fig. S7. FESEM investigations of the top surface microstructure of: (A-C) **ann-TNT-80 (open-top)** and (D) **Ir(8 mM)@TNT-80 (open-top)**.
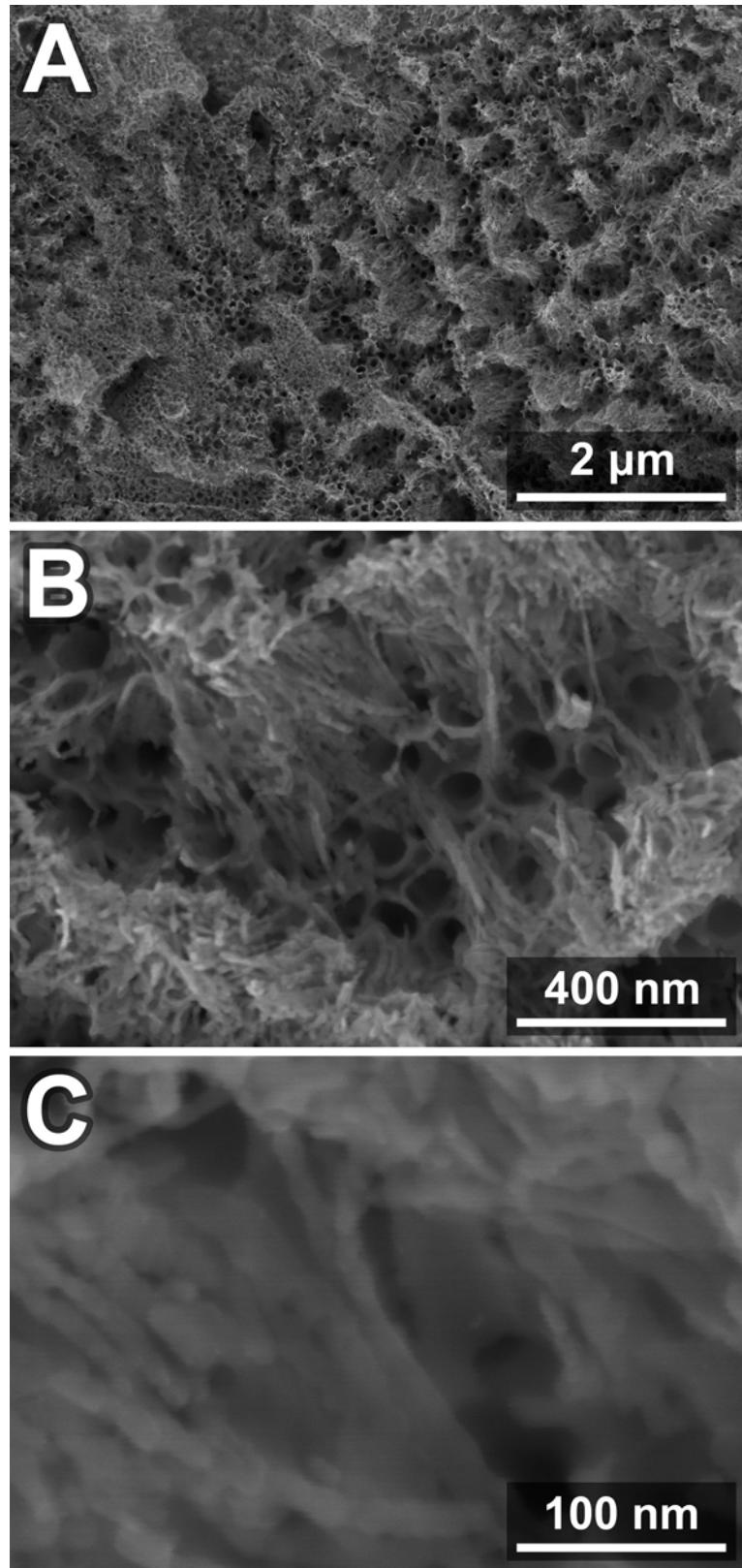
Fig. S8. FESEM analysis of TNT-25 array-based samples: (A and B) Top surface morphology of **ann-TNT-25**; (C) High-magnification top view image of **Ir(0.8 mM)@TNT-25**.

Table S1. Average tube lengths of the TNT-80 and TNT-25 arrays determined by SEM, and the interface capacitances, C_{int}, of the H-TNT-80 and H-TNT-25 electrodes determined at a potential of 1.0 V from CV measurements and at a potential of −0.47 V from EIS measurements.

SEM cross-section		
Sample	Average tube length / µm	Ratio
TNT-80	16.7	2.4
TNT-25	7.1	1
CV measurements, E = 1.0 V		
Sample	C_{int} / mF cm^{-2}	Ratio
H-TNT-80	6.54	2.5
H-TNT-25	2.65	1
EIS measurements, E = −0.47 V		
Sample	C_{int} / mF cm^{-2}	Ratio
H-TNT-80	250	2.5
H-TNT-25	101	1
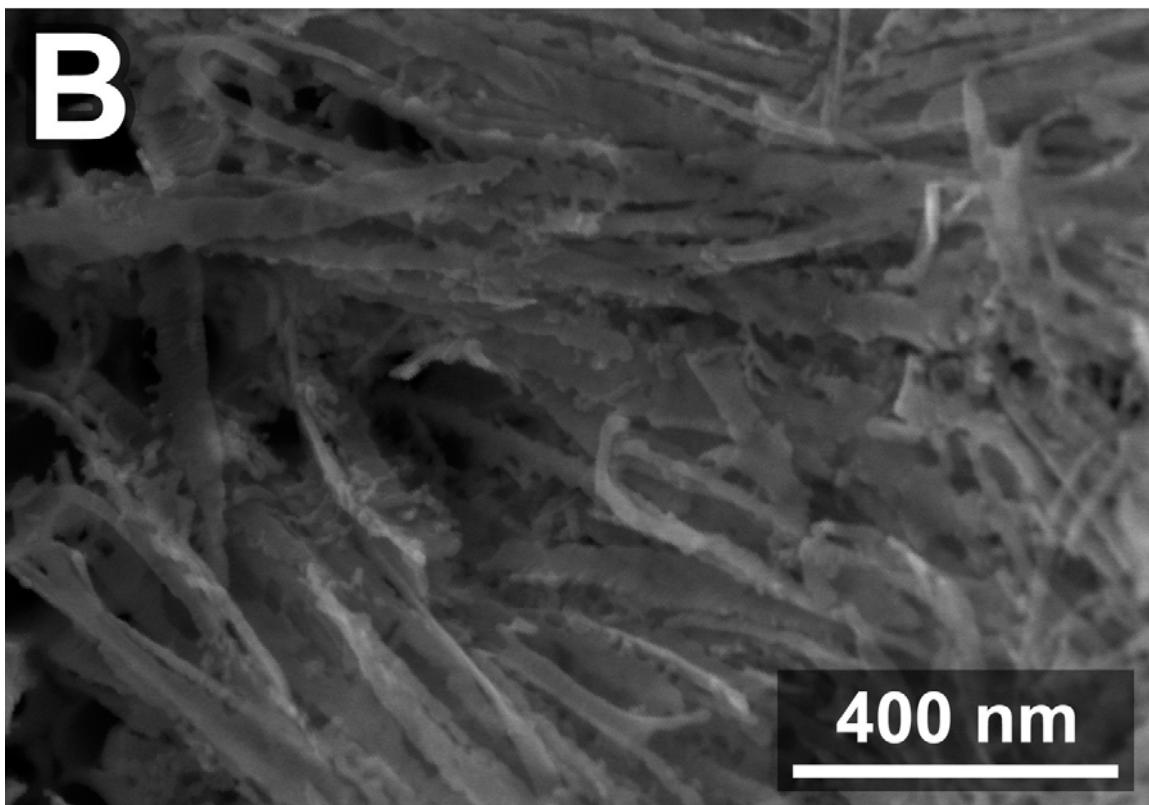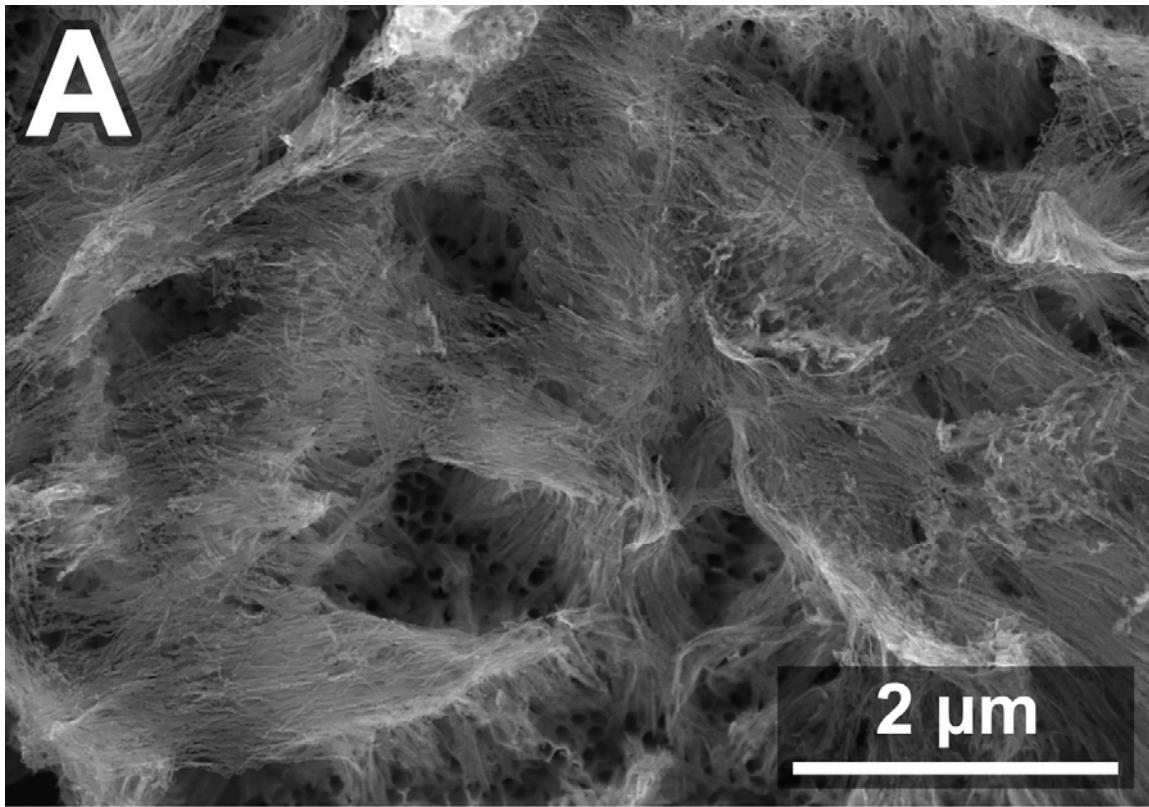
Fig. S9. FESEM images showing the top surface microstructure of **Ir(0.2 mM)@TNT-80** at two different magnifications (A and B).
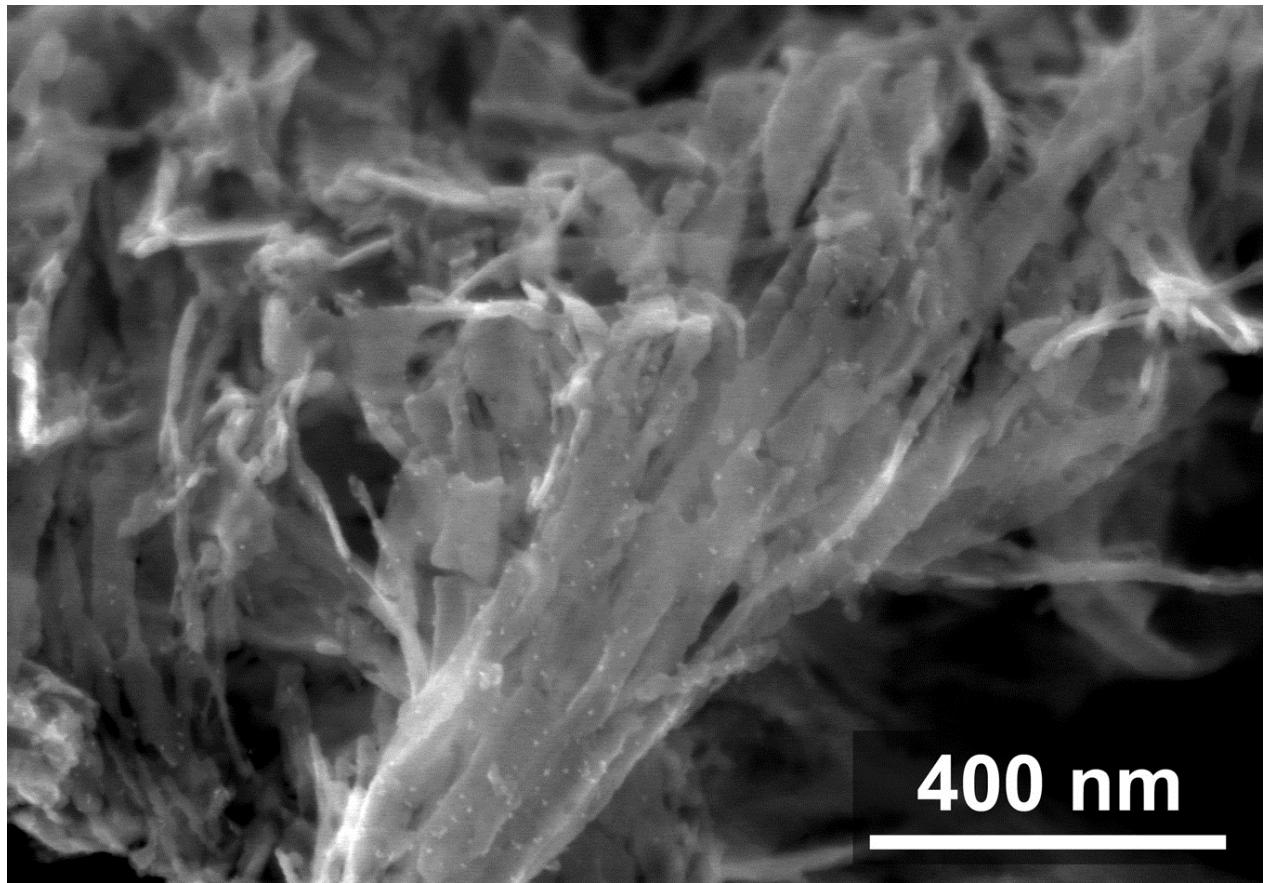
Fig. S10. FESEM image of a nanograss bundle of **Ir(8 mM)@TNT-80**.
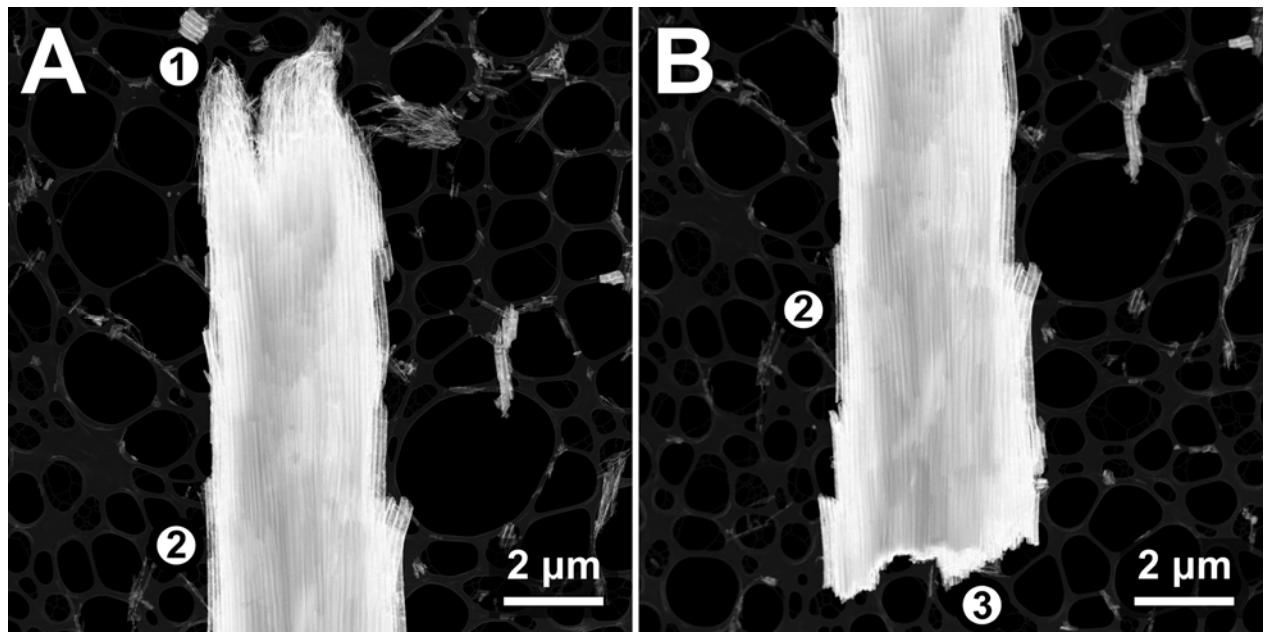
Fig. S11. HAADF-STEM images showing a full-length TNT chunk of the **Ir(8 mM)@TNT-80** sample with marked positions at which EDS mapping analysis was performed.
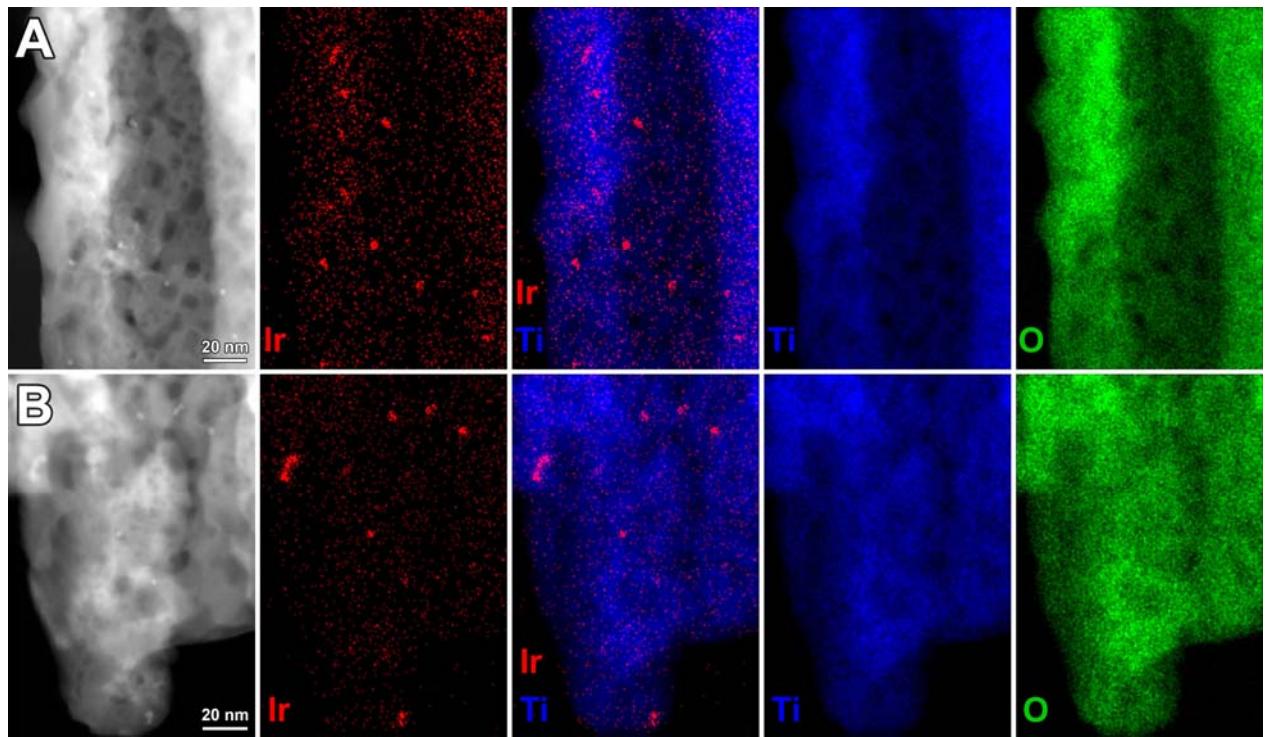
Fig. S12. HAADF-STEM image and corresponding EDS elemental maps of Ir, Ir+Ti, Ti and O acquired from different positions along the **Ir(8 mM)@TNT-80** chunk presented in **Fig. S11**: (A) site 2 – middle and (B) site 3 – bottom.
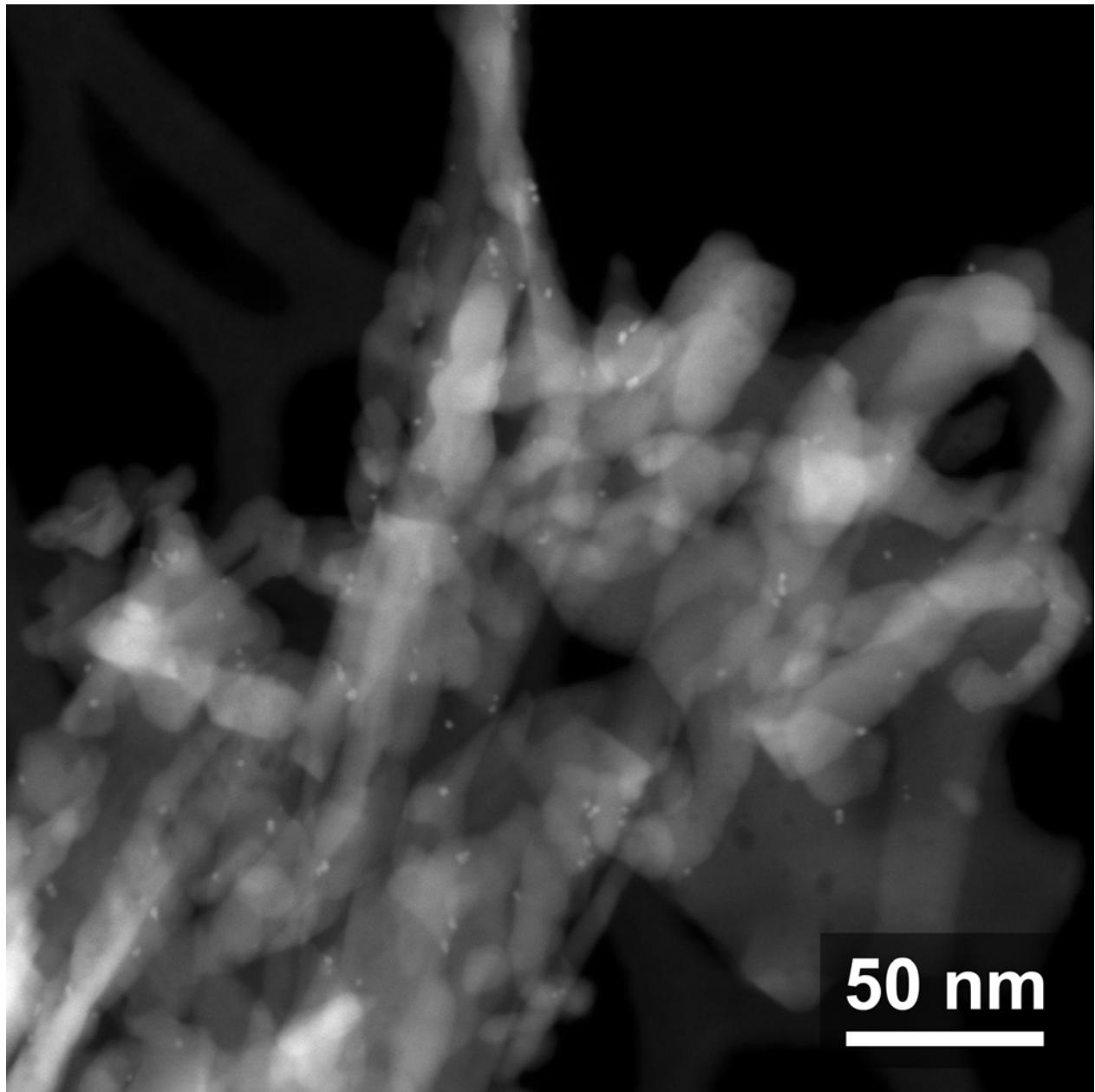
Fig. S13. HAADF-STEM image of a nanograss part of **Ir(0.2 mM)@TNT-80**.
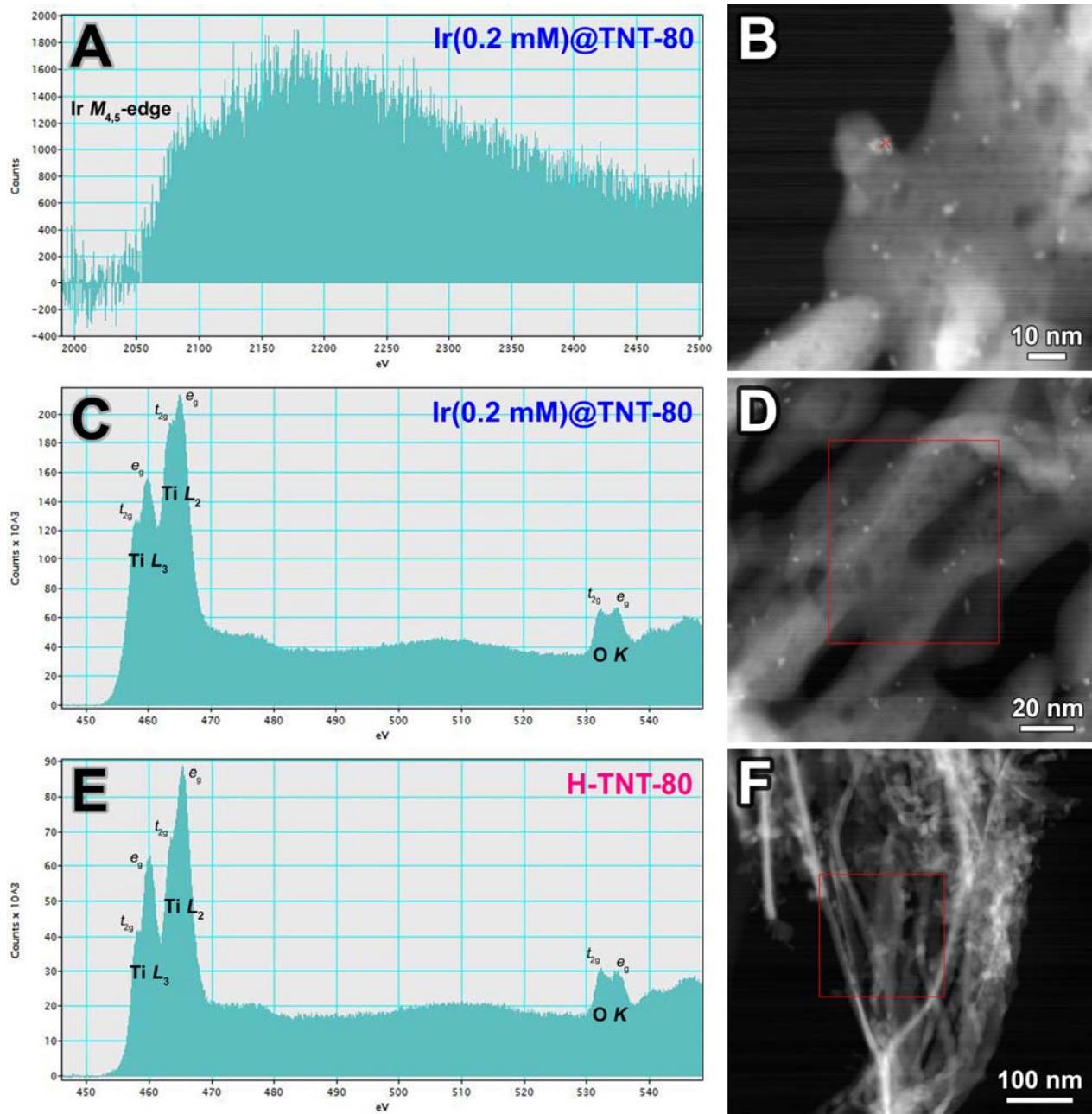
Fig. S14. EEL spectra of **Ir(0.2 mM)@TNT-80** and **H-TNT-80** (A, C and E) together with corresponding HAADF-STEM images showing the locations from which they were acquired (B, D and F, respectively). (A) Iridium $M_{4,5}$ edges of **Ir(0.2 mM)@TNT-80**; Titanium L_2 and L_3 and oxygen K edges of (C) **Ir(0.2 mM)@TNT-80** and (E) **H-TNT-80**.
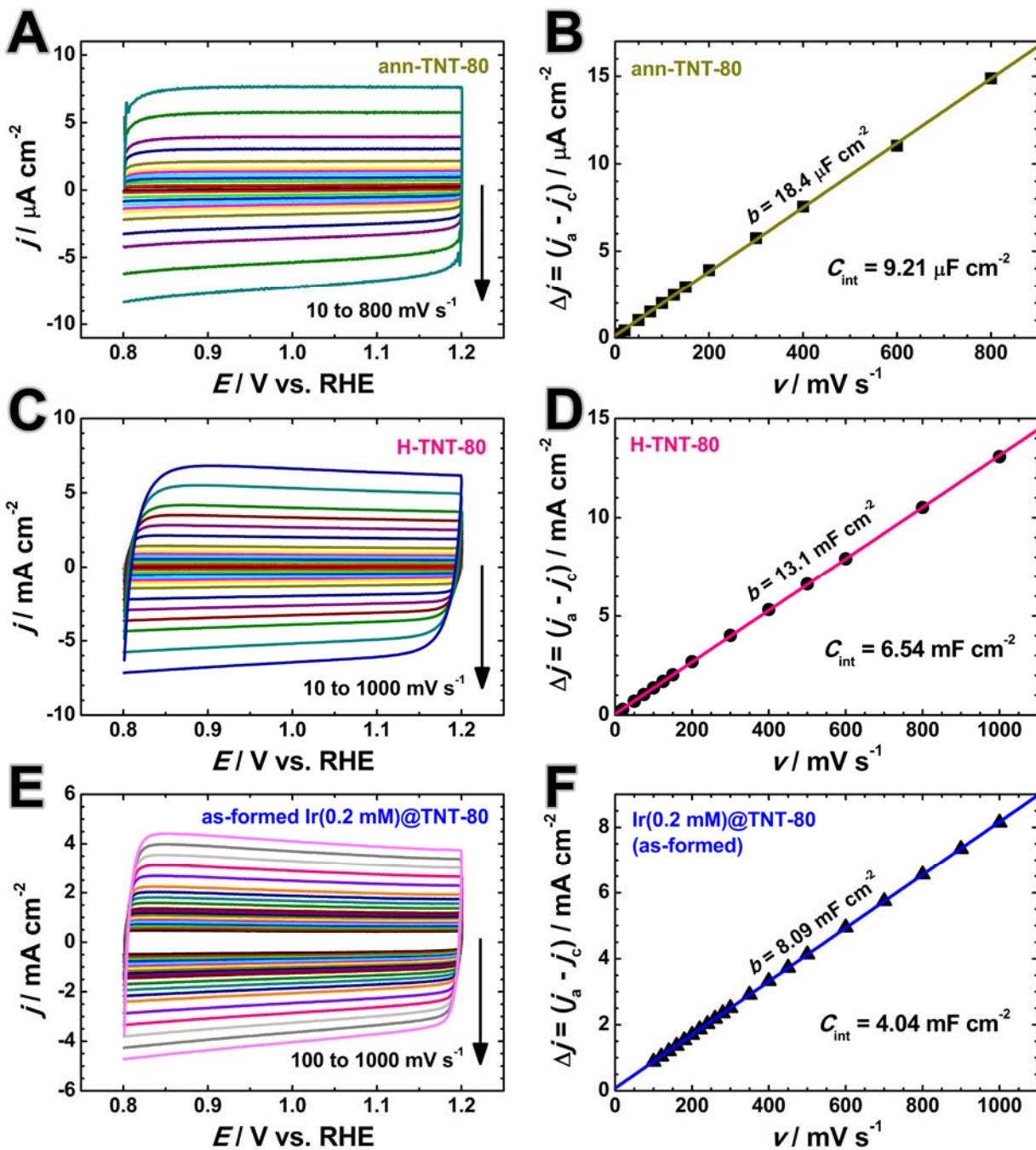
Fig. S15. Cyclic voltammograms recorded in 1 M HClO$_4$ between 0.8 V and 1.2 V at various sweep rates in the range v = 10-1000 mV s^{-1} (A, C and E) and corresponding Δj vs. v plots at 1.0 V (B, D and F, respectively) for: (A and B) **ann-TNT-80**, (C and D) **H-TNT-80** and (E and F) **as-formed Ir(0.2 mM)@TNT-80**.
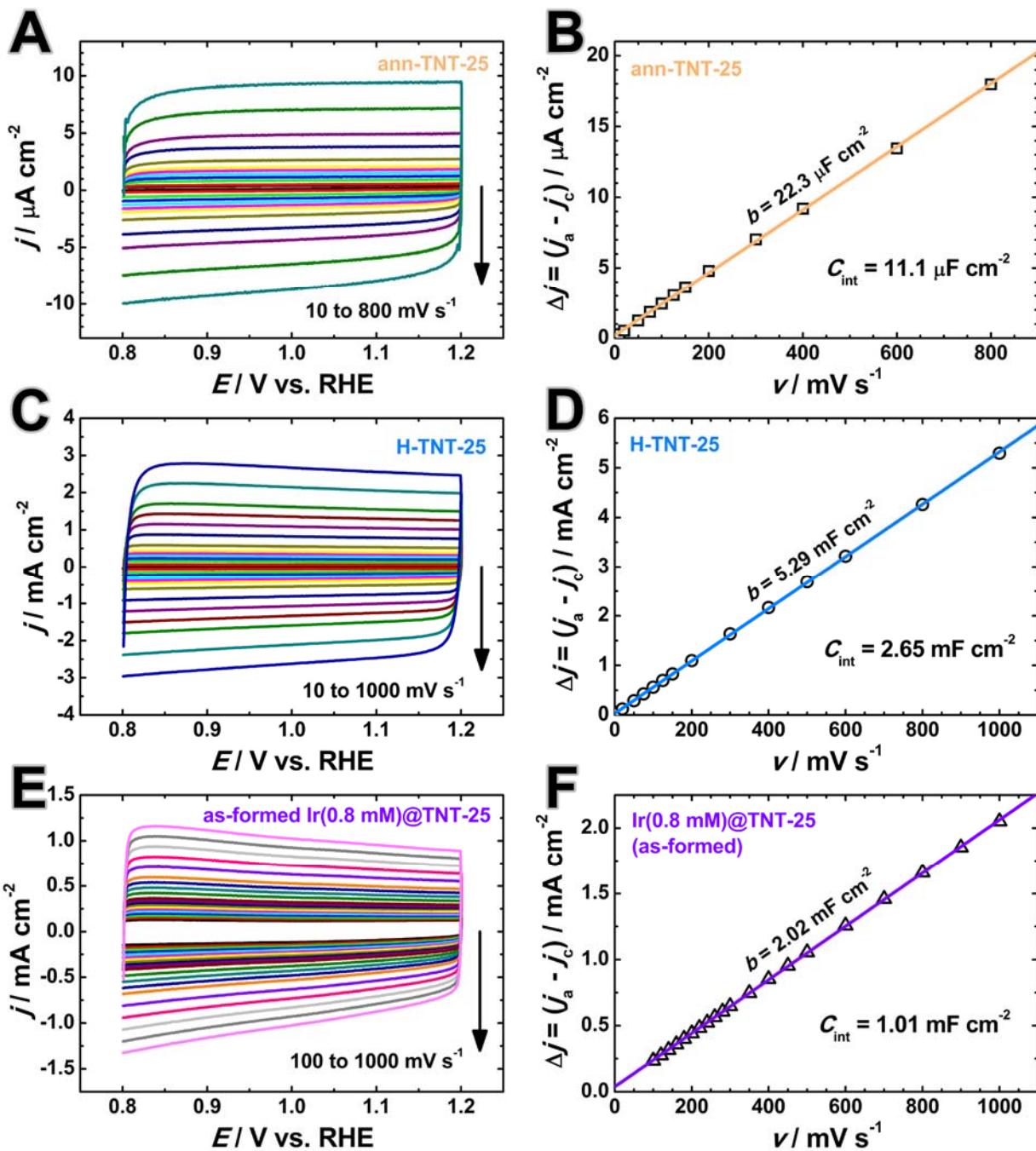
Fig. S16. Cyclic voltammograms recorded in 1 M $HClO_4$ between 0.8 V and 1.2 V at various sweep rates in the range v = 10-1000 mV s^{-1} (A, C and E) and corresponding Δj vs. v plots at 1.0 V (B, D and F, respectively) for: (A and B) **ann-TNT-25**, (C and D) **H-TNT-25** and (E and F) **as-formed Ir(0.8 mM)@TNT-25**.

Supplementary Note 1:

The capacitance values (*C*) that were used for constructing Mott-Schottky plots were extracted from the imaginary component of impedance (*Z''*) at *f* = 2 kHz according to the equation:

$$Z'' = -\frac{1}{\omega \cdot C} = -\frac{1}{2 \cdot \pi \cdot f \cdot C}$$

The donor density (*N*$_D$) was assessed from an adequate slope of the Mott-Schottky plots [N1] by means of the Mott-Schottky equation:

$$N_D = \left(\frac{2}{e \cdot \varepsilon_r \cdot \varepsilon_0} \right) \left[\frac{d\left(C_{int}^{-2}\right)}{dE} \right]^{-1}$$

where *e* = 1.60217662 × 10^{-19} C is the elementary charge, ε_0 = 8.85 × 10^{-12} F m^{-1} is the permittivity of vacuum, ε_r is the relative permittivity of TiO$_2$ (taken as 31 for anatase [N2]), C_{int} is the capacitance of the TNT|electrolyte interface and *E* is the applied potential.

It should be remarked that the Mott-Schottky equation is developed based on models that strictly apply only to bulk semiconductor electrodes with flat surface in the depletion zone. Therefore, Mott-Schottky analysis cannot yield absolute *N*$_D$ values for three-dimensional TNT structures [N3]. In addition, heavily protonated TNT arrays act as degenerate semiconductors, i.e. show metal-like behavior in a wide range of potentials. Consequently, the *N*$_D$ values determined from the Mott-Schottky treatment cannot be considered precise, but still provide a general picture regarding the electronic properties of H-TNT supports.

References:

[N1] A. G. Muñoz, *Electrochim. Acta*, 2007, **52**, 4167–4176.

[N2] H. Tang, K. Prasad, R. Sanjinès, P. E. Schmid and F. Lévy, *J. Appl. Phys.*, 1994, **75**, 2042–2047.

[N3] G. Wang, H. Wang, Y. Ling, Y. Tang, X. Yang, R. C. Fitzmorris, C. Wang, J. Z. Zhang and Y. Li, *Nano Lett.*, 2011, **11**, 3026–3033.
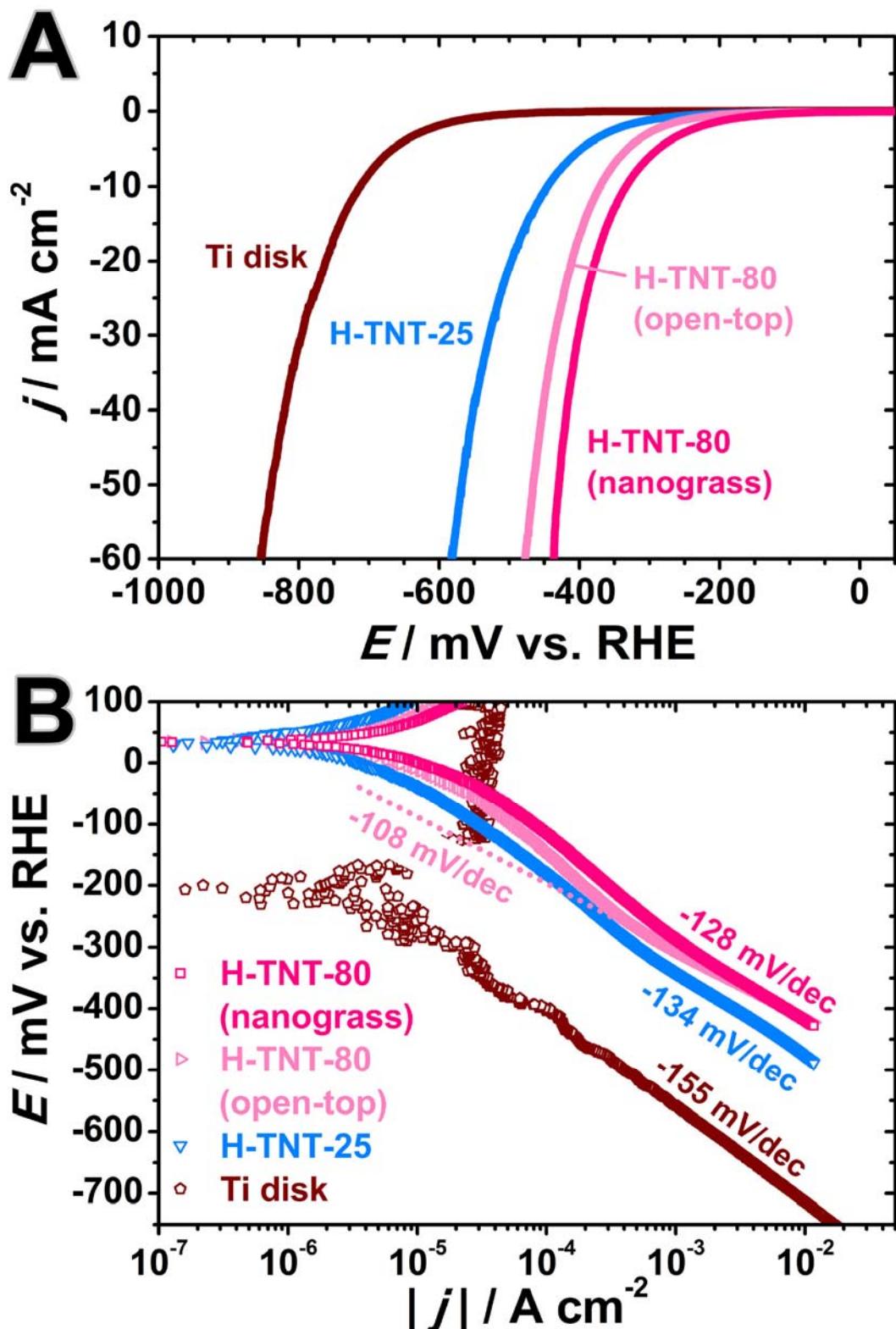
Fig. S17. (A) Polarization curves and (B) Tafel plots of **Ti disk**, **H-TNT-25**, **H-TNT-80 (open-top)** and **H-TNT-80** electrodes. Polarization measurements were performed in H_2-saturated 1 M $HClO_4$ at a sweep rate of 1 mV s^{-1}.

Table S2. HER kinetic and activity parameters for investigated samples determined from polarization measurements: the Tafel slope observed at low current densities, b, and the corresponding exchange current density, j_0; the overpotentials at current densities of -10 mA cm^{-2} and -100 mA cm^{-2}, η_{10} and η_{100}, respectively; the performance degradation after a potential cycling test measured by $|\Delta\eta_{100}|$.

Sample	b / mV dec^{-1}	j_0 / μA cm^{-2}	η_{10} / mV	η_{100} / mV	$|\Delta\eta_{100}|$ after 1000 cycles / mV
Ti disk	−155	0.24	−712		
H-TNT-25	−134	2.8	−446		
H-TNT-80 (open-top)	−108	1.5	−371		
H-TNT-80	−128	5.3	−334		
Ir(8 mM)@TNT-80 (open-top)	−35	380	−59	−166	
Ir(0.8 mM)@TNT-25	−37	730	−39	−77	12
Ir(8 mM)@TNT-80	−35	350	−46	−112	12
Ir(2 mM)@TNT-80	−36	620	−31	−69	5
Ir(0.8 mM)@TNT-80	−36	690	−29	−66	2
Ir(0.2 mM)@TNT-80	−36	730	−27	−63	0
Ir(0.08 mM)@TNT-80	−78	1600	−53	−161	
(Ir/C)@Ti disk	−73	8200	−25	−83	25
(Pt/C)@Ti disk	−36	3800	−24	−56	19

Supplementary Note 2:

The turnover frequency (TOF) is an activity metric that represents the specific activity of an electrode at a given potential and in the case of the HER it is defined as the number of H_2 molecules evolved per active site per second. Therefore, the following general equation can be used for calculating the TOF (units: s^{-1}) of our Ir@TNT composites:

$$TOF = \frac{j}{2 \cdot F \cdot n_s(\text{Ir})}$$

where j is the measured current per geometric surface area of the electrode (units: $A\ cm^{-2}_{geom}$), the factor 2 refers to 2 electrons required to produce one H_2 molecule, F is the Faraday constant (F = 96485 C mol^{-1}) and $n_s(\text{Ir})$ is the total number of moles of Ir active sites per geometric surface area of the electrode (units: mol cm^{-2}_{geom}). We considered the upper and lower bound TOF values of the composites, denoted by TOF_{upp} and TOF_{low}, respectively. The TOF_{low} approximates that all Ir atoms within the Ir@TNT structure are electrochemically accessible. Hence, the TOF_{low} can be calculated from:

$$TOF_{low} = \frac{j}{2 \cdot F} \cdot \frac{M(\text{Ir})}{m_s(\text{Ir})}$$

where $m_s(\text{Ir})$ is the Ir loading at the electrode (units: $\mu g\ cm^{-2}_{geom}$) and M(Ir) is the molar mass of iridium ($M(\text{Ir})$ = 192.217 g mol^{-1}). On the other hand, the TOF_{upp} takes into account that the HER can proceed only at the Ir sites at the surface of Ir nanoparticles. We used the following equation for estimation of the TOF_{upp}:

$$TOF_{upp} = \frac{j}{2 \cdot F} \cdot \frac{N_A}{N_{Ir}(111) \cdot A_{PTCL} \cdot N_s}$$

where $N_{Ir}(111)$ is the number of Ir sites per surface area unit of an Ir nanoparticle under the assumption that it is enclosed only by (111) planes (units: cm^{-2}), A_{PTCL} is the surface area of one Ir nanoparticle (units: cm^2), N_s is the number of Ir nanoparticles per geometric surface area of the electrode (units: cm^{-2}_{geom}) and N_A is the Avogadro constant ($N_A = 6.022 \cdot 10^{23}$ mol^{-1}). A geometric analysis of the fcc (111) surface yields the effective surface area of the (111) plane corresponding to one Ir atom:

$$A_{111} = \frac{\sqrt{3}}{4} a^2$$

where a is the lattice constant of fcc Ir (a = 0.38394 nm, American Mineralogist Crystal Structure Database (AMCSD), http://rruff.geo.arizona.edu/AMS/xtal_data/DIFfiles/13252.txt). $N_{Ir}(111)$ is simply the reciprocal of A_{111}, i.e. $N_{Ir}(111) = 1/A_{111} = 1.57 \cdot 10^{15}$ sites cm^{-2}. We assumed that Ir nanoparticles were hemispheres, so the following expressions were taken to calculate their surface area A_{PTCL} and volume V_{PTCL}:

$$A_{PTCL} = \frac{d^2_{avg} \cdot \pi}{2}$$

$$V_{PTCL} = \frac{d^3_{avg} \cdot \pi}{12}$$

where d_{avg} is the average diameter (units: nm). N_s can be estimated from the following equation:

$$N_s = \frac{m_s(\text{Ir})}{\rho(\text{Ir}) \cdot V_{\text{PTCL}}}$$

where $\rho(\text{Ir})$ is the density of metallic iridium ($\rho(\text{Ir})$ = 22.56 g cm^{-3}). Therefore, in order to plot the overpotential dependencies of TOF$_{\text{upp}}$ and TOF$_{\text{low}}$ for **Ir(0.2 mM)@TNT-80** and **Ir(8 mM)@TNT-80** that are given in **Fig. 5B**, we used j from the polarization curves, while their $m_s(\text{Ir})$ and d_{avg} values were determined by ICP-QMS ($m_s(\text{Ir})$ = 5.7 µg$_{\text{Ir}}$ cm^{-2} and 23 µg$_{\text{Ir}}$ cm^{-2}, respectively) and TEM (d_{avg} = 1.8 nm and 4.5 nm, respectively).
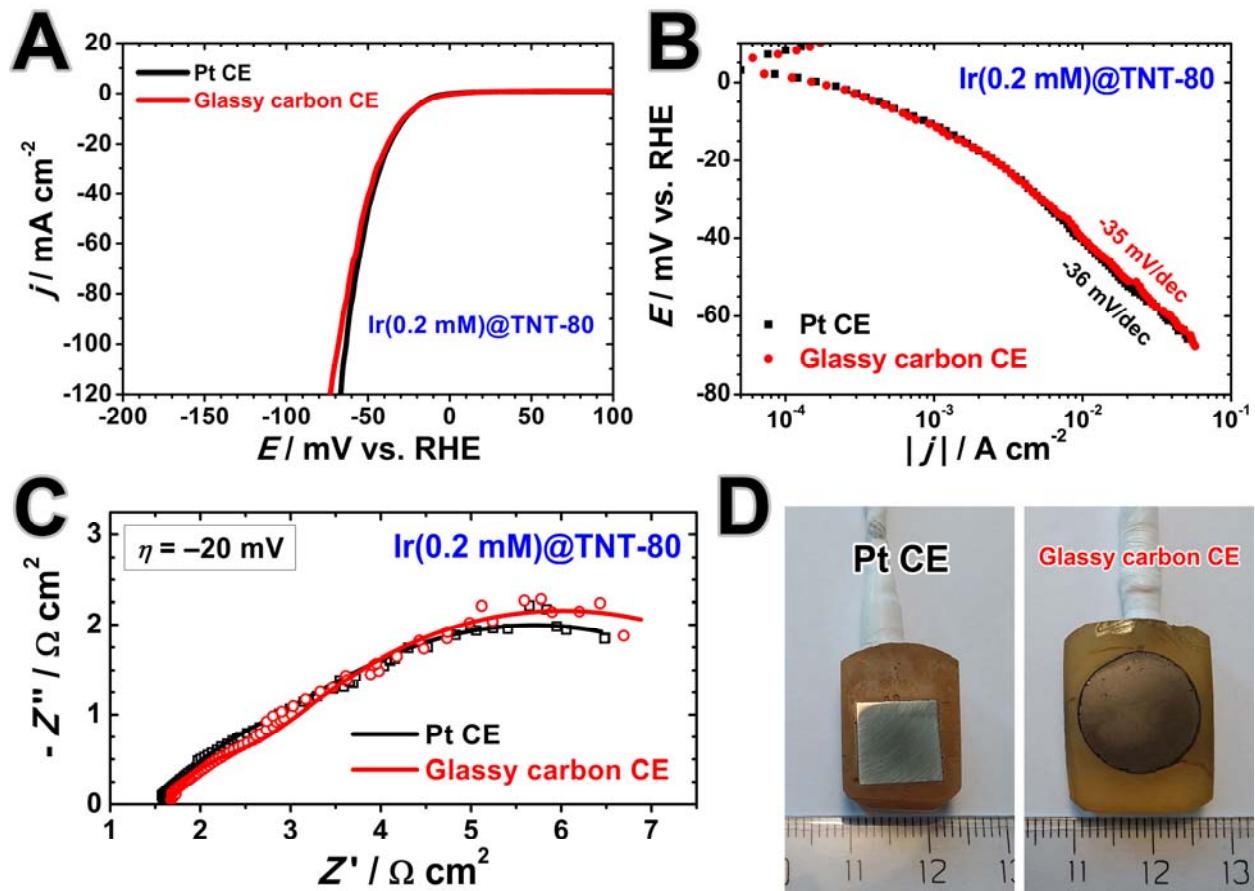
Fig. S18. Electrochemical experiments performed on **Ir(0.2 mM)@TNT-80** using a Pt and glassy carbon counter electrode: (A) polarization curves, (B) Tafel plots and (C) Nyquist curves. (D) Digital photographs of the Pt and glassy carbon counter electrode.

Table S3. Activity and kinetic parameters of recently reported TNT-, Ir- and other PGM- (Rh, Os, Ru, Pd and Pt) based catalysts for the HER in acid solutions, determined from their polarization curves at room temperature.

Catalyst	Solution	Sweep rate/mV s^{-1}	Measured current density/mA cm^{-2}	Overpotential /mV	PGM loading/µg cm^{-2}	Mass activity (at −100 mV)/A mg^{-1}_{PGM}	Tafel slope/mV dec^{-1}	Exchange current density/mA cm^{-2}	Ref.
Ir(0.2 mM)@TNT-80	**1 M HClO$_4$ (H$_2$)**	**1**	**−10** **−50** **−100** **−200**	**−27** **−51** **−63** **−81**	**5.7**	**8.3 at −50 mV** **34 at −80 mV**	**−36**	**0.73**	**This work**
Pd@TNT	1 M HClO$_4$ (H$_2$)	1	−10 −50 −100 −200	−38 −92 −121 −156	12	1.3 at −50 mV 5.0 at −100 mV	−13	0.115	[S1]
RuO$_x$@TNT	1 M HClO$_4$ (H$_2$)	1	−10 −50 −100	−121 −170 −190			−70	0.180	[S2]
MoS$_x$/TNT	0.5 M H$_2$SO$_4$	10	−10	−157			−53		[S3]
MoS$_2$/TNT	0.5 M H$_2$SO$_4$	5	−10	−210			−52		[S4]
IrP$_2$@NC	0.5 M H$_2$SO$_4$	5	−10 −50	−8 −35	77	0.65 at −35 mV	−28		[S5]
IrHNC	0.5 M H$_2$SO$_4$ (N$_2$)	5	−10 −100	−4.5 −39	18	4.2 at −30 mV	−10		[S6]
Ir NP/PC	0.5 M H$_2$SO$_4$ (Ar)	5	−10 −100	−30 −101	58	0.16 at −30 mV	−35		[S7]
AlNiCoIrMo	0.5 M H$_2$SO$_4$	5	−10 −40	−18 −48	24.3		−33		[S8]
Ir$_6$Ag$_9$ nanotubes/C	0.5 M H$_2$SO$_4$ (N$_2$)	5	−10	−20	13.3		−28		[S9]
Ir@N-G-750	0.5 M H$_2$SO$_4$	5	−10 −30	−19 −44	11.5	2.62 at −43 mV	−26		[S10]

Material	Electrolyte		Potential	Overpotential					Ref.
IrNi@OC	0.5 M H_2SO_4 (N_2)	2	−10 −100	−35 −95	15		−18		[S11]
Cucurbit[6]uril-Ir	0.5 M H_2SO_4	10	−10	−54	20		−30		[S12]
Li-IrSe$_2$	0.5 M H_2SO_4 (H_2)	2	−10	−55		0.05 at −50 mV			[S13]
IrFe/NC	0.5 M H_2SO_4 (N_2)	2	−10 −100	−41 −101	68		−22		[S14]
IrW/C	0.1 M $HClO_4$ (N_2)	5	−10	−12	10.2		−22		[S15]
Cube-shaped $Er_2Si_2O_7$:IrO_2	0.5 M H_2SO_4 (N_2)	5	−10	−206	55		−49	0.06	[S16]
Ir nanowires	0.5 M H_2SO_4	5	−10	−15	41		−34		[S17]
Cu_{2-x}S@IrS$_y$@IrRu	0.1 M $HClO_4$ (N_2)	5	−10 −20	−8 −15	13 (Ir+Ru)	2.1 A $mg^{-1}_{(Ir+Ru)}$ at −20 mV	−25		[S18]
IrCo nanodendrites	0.1 M $HClO_4$	5	−10	−17	15		−35		[S19]
Wavy Ir nanowires	0.5 M $HClO_4$ (N_2) 0.1 M $HClO_4$ (N_2)	5	−10 −10	−15 −11	31		−30 −30		[S20]
Ir@CON	0.5 M H_2SO_4 (N_2)	5	−10 −50	−14 −22	102		−27	1.15	[S21]
IrCo@NC	0.5 M H_2SO_4 (N_2)	2	−10 −100	−24 −100	4.3	23	−23		[S22]
Co@Ir/NC	0.5 M H_2SO_4 (N_2)	10	−10 −50	−29 −110	27	1.7	−42		[S23]
IrO_2–TiO_2	0.5 M H_2SO_4 (Ar)	2	−10	−107	10200		−47		[S24]
Ir/graphite foam	0.5 M H_2SO_4 (N_2)	1	−10 −200	−7 −61	820	0.2 at −50 mV	−30		[S25]
IrNi$_{0.57}$Fe$_{0.82}$/C	0.5 M $HClO_4$	5	−10 −30	−24 −62	92	0.25 at −50 mV	−35		[S26]
IrCo-PHNC	0.1 M $HClO_4$ (N_2)	5	−10 −20	−21 −35	10.0	3.2 at −50 mV	−27		[S27]

Catalyst	Electrolyte								Ref.
IrNi nanoclusters	0.1 M $HClO_4$ (N_2) 0.5 M H_2SO_4 (N_2)	5	−20	−21 −32	12.5				[S28]
Rh NP/PC	0.5 M H_2SO_4 (Ar)	5	−10 −100	−21 −50	55	0.53 at −30 mV	−34		[S7]
Rh–Rh_2O_3-NPs/C	0.5 M H_2SO_4 (N_2)	10	−10 −100	−14 −103	28	3.4	−32	4.2	[S29]
Rh/F-graphene	0.5 M H_2SO_4	5	−10	−46	10.6	2.1 at −50 mV	−30	0.3	[S30]
PAH@Rh-NSNSs/CNT	0.5 M H_2SO_4 (N_2)	5	−10 −100	−5 −24	52		−30		[S31]
Wrinkled Rh_2P nanosheets/C	0.1 M $HClO_4$ (N_2)	5	−10	−16	10.7		−30		[S32]
Rh_xP/NPC	0.5 M H_2SO_4 (Ar)	10	−10 −50	−19 −80	1.6	39 (in 0.1 M $HClO_4$)	−36		[S33]
Rh_2P	0.5 M H_2SO_4	5	−10 −50	−14 −56	130	0.34 at −50 mV	−32		[S34]
B-doped RhFe	0.5 M H_2SO_4 (N_2)	5	−10 −60	−25 −101	55	1.1	−32	1.91	[S35]
Rh-Au-Si NWs	0.5 M H_2SO_4 (N_2)	5	−10	−62	78 (Rh+Au)	3.1 A $mg^{-1}_{(Rh+Au)}$ at −300 mV	−24	0.048	[S36]
Rh–Ag/Si NWs	0.5 M H_2SO_4 (N_2)	5	−10	−120	3.2	11.5 at −200 mV	−51	0.087	[S37]
Rh–MoS_2	0.5 M H_2SO_4 (N_2)	5	−10	−47	16.1	13.9 at −250 mV	−24	0.114	[S38]
Rh/Si NWs	0.5 M H_2SO_4 (N_2)	5	−100	−180	56.2	1.8 at −180 mV	−24	0.0086	[S39]
Hollow Rh_2S_3 nanoprisms	0.5 M H_2SO_4 (N_2)	2	−10	−122	13.6	0.3	−44		[S40]
Os-Ag-Si	0.5 M H_2SO_4 (Ar)	5	−10 −100	−57 −152	42	1.2	−27		[S41]
Os/Si NWs	0.5 M H_2SO_4 (N_2)	5	−10 −100	−43 −68	83	3.7	−24	0.464	[S42]

Ru NP/PC	0.5 M H_2SO_4 (Ar)	5	−10 −100	−81 −164	50	0.031 at −30 mV	−63		[S7]
Octahedral Pd@RuO$_x$	0.5 M H_2SO_4	2	−10	−33	10 (Pd+Ru)	2.2 A mg^{-1}$_{(Pd+Ru)}$ at −50 mV	−33		[S43]
Ru@NG	0.5 M H_2SO_4 (Ar)	2	−10 −50	−43 −100	201	0.25	−55	0.21	[S44]
Mo$_2$C@Ru	0.5 M H_2SO_4 (N$_2$)	5	−10 −50	−25 −66	21	1.5 at −50 mV			[S45]
Ru-CCS	0.5 M H_2SO_4 (H$_2$)	2	−10 −50	−27 −57	11	3.9 at −50 mV	−33	1.3	[S46]
NiRu@N−C	0.5 M H_2SO_4	5	−10	−50	5.1	2.0 at −50 mV	−36		[S47]
Ni@Ni$_2$P−Ru	0.5 M H_2SO_4 (N$_2$)	5	−10	−51	23	0.4 at −50 mV	−35	0.32	[S48]
RuCoP	0.5 M H_2SO_4 (Ar/H$_2$)	5	−10 −50 −100	−11 −47 −77	53	1.0 at −50 mV	−31		[S49]
RuP$_x$@NPC	0.5 M H_2SO_4	2	−10	−51	25	2.7	−46		[S50]
Ru−C$_3$N$_4$/rGO	0.5 M H_2SO_4 (N$_2$)		−10	−80	20	0.8	−55	0.46	[S51]
Ru$_2$P/rGO	0.5 M H_2SO_4 (N$_2$)	5	−10	−22	46		−29	2.2	[S52]
Ru/CeO2	0.5 M H_2SO_4 (N$_2$)	5	−10 −50	−47 −117	197	0.2	−41	0.67	[S53]
W + Ru/C + BP$_{2000}$	0.5 M H_2SO_4	2	−10	−85	5.6		−46		[S54]
Cu$_{2−x}$S@Ru/C	0.5 M H_2SO_4 (N$_2$)	2	−10	−129	29	0.2	−51		[S55]
Ru@C$_2$N	0.5 M H_2SO_4 (N$_2$)	5	−10	−22	82	0.4 at −50 mV	−30	1.9	[S56]
Ru−MoO$_2$	0.5 M H_2SO_4 (N$_2$)	2	−10	−55	92	0.09 at −50 mV	−44		[S57]
Ni$_{1.5}$Co$_{1.4}$P@Ru	0.5 M H_2SO_4 (N$_2$)		−10	−49			−49	1.26	[S58]

Ru/MeOH/THF	0.5 M H_2SO_4 (Ar)	10	−10	−83			−46		[S59]
Ru/NG	0.5 M H_2SO_4	5	−10	−53	15	2.9	−44		[S60]
RuP$_2$/NPC	0.5 M H_2SO_4	5	−10	−38	233	0.07 at −50 mV	−38	2.0	[S61]
NiCo$_2$S$_4$/Pd	0.5 M H_2SO_4	5	−10	−83	43	0.37	−70		[S62]
Pd$_{13}$Cu$_3$S$_7$	0.5 M H_2SO_4 (N$_2$)	5	−10	−64	15	2.0	−50		[S63]
PdP$_2$@CB	0.5 M H_2SO_4 (N$_2$)	5	−10 −100	−28 −150			−30		[S64]
Pd-Si NWs	0.5 M H_2SO_4 (N$_2$)	5	−10	−153	56	0.8 at −250 mV	−70		[S65]
Pd/Ti$_2$AlC	0.5 M H_2SO_4	1	−10 −50 −100	−27 −50 −73	25.4	8.1	−64	6.8	[S66]
Ag@AgPd nanocubes	0.5 M H_2SO_4 (Ar)	2	−10	−93	3.2	4.3	−70		[S67]
Pd/OMC	0.5 M H_2SO_4	20	−5	−215	1.15	3.2 at −200 mV	−111		[S68]
Pd nanocubes/PEI−rGO	0.5 M H_2SO_4	5	−100	−94	14	7.7	−34	1.10	[S69]
Pd nanodisks/defect-rich MoS$_2$	0.5 M H_2SO_4 (N$_2$)		−10	−103			−41	0.427	[S70]
Pd−Mn$_3$O$_4$	0.5 M H_2SO_4	2	−10 −100	−14 −195	19	2.1	−42	7.74	[S71]
Pd$_4$Se	0.5 M H_2SO_4 (N$_2$)	2	−10	−94	169	0.070	−50	0.23	[S72]
Pd−CN$_x$	0.5 M H_2SO_4 (N$_2$)	10	−10 −50	−55 −87	43	1.4	−35	0.40	[S73]
PdCo@CN	0.5 M H_2SO_4 (N$_2$)		−10	−80			−31		[S74]
Pd$_{3.02}$Te nanowires/rGO	0.5 M H_2SO_4	5	−10	−48	71.2	0.48	−63	1.81	[S75]
Pd−Au/carbon fiber paper	0.5 M H_2SO_4 (N$_2$)	5	−100	−204	500 (Pd+Au)	0.032 A mg$^{-1}_{(Pd+Au)}$	−47	0.256	[S76]

Pd–MoS$_2$	0.5 M H$_2$SO$_4$	1	−100	−415	229	0.19 at −300 mV	−45	0.0046	[S77]
Ni@Pd/PEI–rGO	0.5 M H$_2$SO$_4$	5	−100 −200	−133 −150	14 (Ni+Pd)		−54	3.91	[S78]
Au–Pd/rGO	0.5 M H$_2$SO$_4$ (Ar)	5	−10	−52			−29	0.47	[S79]
PdPS–rGO	0.5 M H$_2$SO$_4$	1	−10	−90	778	0.015	−46	0.14	[S80]
Pt/NiS@Al$_2$O$_3$	0.5 M H$_2$SO$_4$	5	−10 −50	−34 −82	16	5.0	−35		[S81]
Pt–Pd@NPA	0.5 M H$_2$SO$_4$ (H$_2$)	5	−10 −100	−28 −58	37.5 (Pt+Pd)	11 A mg^{-1}$_{(Pt+Pd)}$	−31	1.78	[S82]
Dendrite-like Pt crystals	0.5 M H$_2$SO$_4$ (Ar)	5	−10 −100	−15 −72	280	0.22 at −50 mV	−31		[S83]
HCS-N-Pt	0.5 M H$_2$SO$_4$ (N$_2$)	5	−10 −100	−14 −40	1.7	59 at −40 mV	−22		[S84]
Hollow (Pt/NiO/RuO$_2$)/C	0.1 M HClO$_4$ (H$_2$)	2	−10	−30	14 (Pt+Ru)	4.9 A mg^{-1}$_{Pt}$ at −50 mV	−35		[S85]
Pt@MoS$_2$/NiS$_2$	0.5 M H$_2$SO$_4$	2	−10	−34	14	7.7	−41		[S86]
Pd$_{86}$Pt$_{14}$ nanowires	0.5 M H$_2$SO$_4$	5	−10 −50	−0.8 −5.4	85 (Pt+Pd)		−29		[S87]
Pd nanomeshes/Pt	0.5 M H$_2$SO$_4$ (N$_2$)	5	−10 −50	−21 −36	20 (Pt+Pd)	5.4 A mg^{-1}$_{(Pt+Pd)}$ at −50 mV	−27		[S88]
Edge-rich WS$_2$-Pt	0.5 M H$_2$SO$_4$	2	−10	−39			−27		[S89]
Pt–MoO$_2$/MWCNTs	0.5 M H$_2$SO$_4$ (H$_2$)	5	−10	−60	2.4	12	−43	0.93	[S90]
PyPOP-Pt@G	1 M H$_2$SO$_4$ (N$_2$)	10	−100	−122	67	0.373 at −50 mV 1.13 at −100 mV	−37		[S91]
PtAgCo nanosheets	0.5 M H$_2$SO$_4$ (N$_2$)	2	−100	−59			−27		[S92]

PtSe$_2$ film (76 nm)	0.5 M H$_2$SO$_4$		−10	−327			−47	0.015	[S93]
Pt@NHPCP	0.1 M HClO$_4$	5	−10	−57	2.0	9.5	−27		[S94]
Pt NC/N-graphene	0.5 M H$_2$SO$_4$ (N$_2$)	5	−10 −100	−24 −84	5.6	7.8 at −50 mV	−28	0.989	[S95]
Pt/SnS$_2$	0.5 M H$_2$SO$_4$ (N$_2$)	10	−10	−117			−69	0.394	[S96]
Pd/Cu-Pt nanorings	0.5 M H$_2$SO$_4$ (N$_2$)	5	−10	−23		3.0 A mg$^{-1}_{(Pt+Pd)}$ at −50 mV	−25		[S97]
Pt–Au–Si NWs	0.5 M H$_2$SO$_4$ (N$_2$)	5	−100	−157	92 (Pt+Au)	0.94 A mg$^{-1}_{Pt}$ at −50 mV	−24	0.073	[S98]
MoS$_2$@Pt	0.5 M H$_2$SO$_4$ (H$_2$)	5	−10	−70	17		−36	0.43	[S99]
Pt-VGNSAs/CC	0.5 M H$_2$SO$_4$ (Ar)	5	−10	−60	42	0.52	−28		[S100]
Pd@Pt NPs/rGO	0.5 M H$_2$SO$_4$ (N$_2$)	5	−10	−56	72 (Pt+Pd)		−39		[S101]
Pt$_{tripods}$@PAA	0.5 M H$_2$SO$_4$ (N$_2$)	2	−150	−47	81	3.8	−26		[S102]
Pt/NPC	0.5 M H$_2$SO$_4$ (H$_2$)	50	−20	−22	5.1	26.4 at −40 mV	−36		[S103]
ALDPt/NGNs	0.5 M H$_2$SO$_4$ (N$_2$)	2	−10	−40	1.1	10.1 at −50 mV	−29		[S104]
Concave octahedral Pd@PdPt nanocrystals	0.5 M H$_2$SO$_4$ (N$_2$)	2	−10	−39	283 (Pt+Pd)	0.035 A mg$^{-1}_{(Pt+Pd)}$ at −39 mV	−38	0.91	[S105]
CuPdPt/C	0.5 M H$_2$SO$_4$	5	−10	−55			−25	0.07	[S106]
Pt–Pd–rGO	0.5 M H$_2$SO$_4$ (Ar)	2	−100	−68	17.5 (Pt+Pd)	10.5 A mg$^{-1}_{(Pt+Pd)}$	−10		[S107]
PtPd–WC/C	0.5 M H$_2$SO$_4$	5	−10	−29	100 (Pt+Pd)	4.3 A mg$^{-1}_{(Pt+Pd)}$	−21	0.414	[S108]

References

[S1] U. Lačnjevac, R. Vasilić, T. Tokarski, G. Cios, P. Żabiński, N. Elezović and N. Krstajić, *Nano Energy*, 2018, **47**, 527–538.

[S2] U. Č. Lačnjevac, V. V. Radmilović, V. R. Radmilović and N. V. Krstajić, *Electrochim. Acta*, 2015, **168**, 178–190.

[S3] Z. Liu, X. Zhang, B. Wang, M. Xia, S. Gao, X. Liu, A. Zavabeti, J. Z. Ou, K. Kalantar-Zadeh and Y. Wang, *J. Phys. Chem. C*, 2018, **122**, 12589–12597.

[S4] C. Meng, Z. Liu, T. Zhang and J. Zhai, *Green Chem.*, 2015, **17**, 2764–2768.

[S5] Z. Pu, J. Zhao, I. S. Amiinu, W. Li, M. Wang, D. He and S. Mu, *Energy Environ. Sci.*, 2019, **12**, 952–957.

[S6] F. Li, G.-F. Han, H.-J. Noh, J.-P. Jeon, I. Ahmad, S. Chen, C. Yang, Y. Bu, Z. Fu, Y. Lu and J.-B. Baek, *Nat. Commun.*, 2019, **10**, 4060.

[S7] M. Ming, Y. Zhang, C. He, L. Zhao, S. Niu, G. Fan and J.-S. Hu, *Small*, 2019, **15**, 1903057.

[S8] Z. Jin, J. Lv, H. Jia, W. Liu, H. Li, Z. Chen, X. Lin, G. Xie, X. Liu, S. Sun and H.-J. Qiu, *Small*, 2019, 1904180.

[S9] M. Zhua, Q. Shao, Y. Qian and X. Huang, *Nano Energy*, 2019, **56**, 330–337.

[S10] X. Wu, B. Feng, W. Li, Y. Niu, Y. Yu, S. Lu, C. Zhong, P. Liu, Z. Tian, L. Chen, W. Hu and C. M. Li, *Nano Energy*, 2019, **62**, 117–126.

[S11] S. Gong, C. Wang, P. Jiang, K. Yang, J. Lu, M. Huang, S. Chen, J. Wang and Q. Chen, *J. Mater. Chem. A*, 2019, **7**, 15079–15088.

[S12] H. You, D. Wu, Z. Chen, F. Sun, H. Zhang, Z. Chen, M. Cao, W. Zhuang and R. Cao, *ACS Energy Lett.*, 2019, **4**, 1301–1307.

[S13] T. Zheng, C. Shang, Z. He, X. Wang, C. Cao, H. Li, R. Si, B. Pan, S. Zhou and J. Zeng, *Angew. Chem. Int. Ed.*, 2019, **58**, 14764–14769.

[S14] P. Jiang, H. Huang, J. Diao, S. Gong, S. Chen, J. Lu, C. Wang, Z. Sun, G. Xia, K. Yang, Y. Yang, L. Wei and Q. Chen, *Appl. Catal. B Environ.*, 2019, **258**, 117965.

[S15] F. Lv, J. Feng, K. Wang, Z. Dou, W. Zhang, J. Zhou, C. Yang, M. Luo, Y. Yang, Y. Li, P. Gao and S. Guo, *ACS Cent. Sci.*, 2018, **4**, 1244–1252.

[S16] P. Karfa, K. C. Majhi and R. Madhuri, *ACS Catal.*, 2018, **8**, 8830–8843.

[S17] J. Yang, Y. Ji, Q. Shao, N. Zhang, Y. Li and X. Huang, *Adv. Funct. Mater.*, 2018, **28**, 1803722.

[S18] J. Joo, H. Jin, A. Oh, B. Kim, J. Lee, H. Baik, S. H. Joo and K. Lee, *J. Mater. Chem. A*, 2018, **6**, 16130–16138.

[S19] L. Fu, X. Zeng, G. Cheng and W. Luo, *ACS Appl. Mater. Interfaces*, 2018, **10**, 24993–24998.

[S20] L. Fu, F. Yang, G. Cheng and W. Luo, *Nanoscale*, 2018, **10**, 1892–1897.

[S21] J. Mahmood, M. A. R. Anjum, S.-H. Shin, I. Ahmad, H.-J. Noh, S.-J. Kim, H. Y. Jeong, J. S. Lee and J.-B. Baek, *Adv. Mater.*, 2018, **30**, 1805606.

[S22] P. Jiang, J. Chen, C. Wang, K. Yang, S. Gong, S. Liu, Z. Lin, M. Li, G. Xia, Y. Yang, J. Su and Q. Chen, *Adv. Mater.*, 2018, **30**, 1705324.

[S23] D. Li, Z. Zong, Z. Tang, Z. Liu, S. Chen, Y. Tian and X. Wang, *ACS Sustainable Chem. Eng.*, 2018, **6**, 5105–5114.

[S24] M. Yuan, Y. Zhu, L. Deng, R. Ming, A. Zhang, W. Li, B. Chai and Z. Ren, *New J. Chem.*, 2017, **41**, 6152–6159.

[S25] J. Zhang, G. Wang, Z. Liao, P. Zhang, F. Wang, X. Zhuang, E. Zschech and X. Feng, *Nano Energy*, 2017, **40**, 27–33.

[S26] L. Fu, G. Cheng and W. Luo, *J. Mater. Chem. A*, 2017, **5**, 24836–24841.

[S27] J. Feng, F. Lv, W. Zhang, P. Li, K. Wang, C. Yang, B. Wang, Y. Yang, J. Zhou, F. Lin, G.-C. Wang and S. Guo, *Adv. Mater.*, 2017, **29**, 1703798.

[S28] Y. Pi, Q. Shao, P. Wang, J. Guo and X. Huang, *Adv. Funct. Mater.*, 2017, **27**, 1700886.

[S29] M. K. Kundu, R. Mishra, T. Bhowmik and S. Barman, *J. Mater. Chem. A*, 2018, **6**, 23531–23541.

[S30] W. Shen, L. Ge, Y. Sun, F. Liao, L. Xu, Q. Dang, Z. Kang and M. Shao, *ACS Appl. Mater. Interfaces*, 2018, **10**, 33153–33161.

[S31] J. Bai, S.-H. Xing, Y.-Y. Zhu, J.-X. Jiang, J.-H. Zeng and Y. Chen, *J. Power Sources*, 2018, **385**, 32–38.

[S32] K. Wang, B. Huang, F. Lin, F. Lv, M. Luo, P. Zhou, Q. Liu, W. Zhang, C. Yang, Y. Tang, Y. Yang, W. Wang, H. Wang and S. Guo, *Adv. Energy Mater.*, 2018, **8**, 1801891.

[S33] Q. Qin, H. Jang, L. Chen, G. Nam, X. Liu and J. Cho, *Adv. Energy Mater.*, 2018, **8**, 1801478.

[S34] F. Yang, Y. Zhao, Y. Du, Y. Chen, G. Cheng, S. Chen and W. Luo, *Adv. Energy Mater.*, 2018, **8**, 1703489.

[S35] L. Zhang, J. Lu, S. Yin, L. Luo, S. Jing, A. Brouzgou, J. Chen, P. K. Shen and P. Tsiakaras, *Appl. Catal. B Environ.*, 2018, **230**, 58–64.

[S36] B. Jiang, L. Yang, F. Liao, M. Sheng, H. Zhao, H. Lin and M. Shao, *Nano Res.*, 2017, **10**, 1749–1755.

[S37] B. Jiang, Y. Sun, F. Liao, W. Shen, H. Lin, H. Wang and M. Shao, *J. Mater. Chem. A*, 2017, **5**, 1623–1628.

[S38] Y. Cheng, S. Lu, F. Liao, L. Liu, Y. Li and M. Shao, *Adv. Funct. Mater.*, 2017, **27**, 1700359.

[S39] L. Zhu, H. Lin, Y. Li, F. Liao, Y. Lifshitz, M. Sheng, S.-T. Lee and M. Shao, *Nat. Commun.*, 2016, **7**, 12272.

[S40] D. Yoon, B. Seo, J. Lee, K. S. Nam, B. Kim, S. Park, H. Baik, S. H. Joo and K. Lee, *Energy Environ. Sci.*, 2016, **9**, 850–856.

[S41] K. Yin, S. Zhang, Y. Sun, H. Huang, Y. Cheng, F. Liao and M. Shao, *J. Colloid Interf. Sci.*, 2019, **539**, 257–262.

[S42] Y. Cheng, X. Fan, F. Liao, S. Lu, Y. Li, L. Liu, Y. Li, H. Lin, M. Shao and S.-T. Lee, *Nano Energy*, 2017, **39**, 284–290.

[S43] L. Zhang, Z.-J. Zhao, M. N. Banis, L. Li, Y. Zhao, Z. Song, Z. Wang, T.-K. Sham, R. Li, M. Zheng, J. Gong and X. Sun, *J. Mater. Chem. A*, 2018, **6**, 24397–24406.

[S44] J. Yang, H. Guo, S. Chen, Y. Li, C. Cai, P. Gao, L. Wang, Y. Zhang, R. Sun, X. Niu and Z. Wang, *J. Mater. Chem. A*, 2018, **6**, 13859–13866.

[S45] Z. Zhang, P. Li, Q. Feng, B. Wei, C. Deng, J. Fan, H. Li and H. Wang, *ACS Appl. Mater. Interfaces*, 2018, **10**, 32171–32179.

[S46] D. Luo, B. Zhou, Z. Li, X. Qin, Y. Wen, D. Shi, Q. Lu, M. Yang, H. Zhou and Y. Liu, *J. Mater. Chem. A*, 2018, **6**, 2311–2317.

[S47] Y. Xu, S. Yin, C. Li, K. Deng, H. Xue, X. Li, H. Wang and L. Wang, *J. Mater. Chem. A*, 2018, **6**, 1376–1381.

[S48] Y. Liu, S. Liu, Y. Wang, Q. Zhang, L. Gu, S. Zhao, D. Xu, Y. Li, J. Bao and Z. Dai, *J. Am. Chem. Soc.*, 2018, **140**, 2731–2734.

[S49] J. Xu, T. Liu, J. Li, B. Li, Y. Liu, B. Zhang, D. Xiong, I. Amorim, W. Li and L. Liu, *Energy Environ. Sci.*, 2018, **11**, 1819–1827.

[S50] J.-Q. Chi, W.-K. Gao, J.-H. Lin, B. Dong, K.-L. Yan, J.-F. Qin, B. Liu, Y.-M. Chai and C.-G. Liu, *ChemSusChem*, 2018, **11**, 743–.

[S51] Y. Peng, W. Pan, N. Wang, J.-E. Lu and S. Chen, *ChemSusChem*, 2018, **11**, 130–136.

[S52] T. Liu, S. Wang, Q. Zhang, L. Chen, W. Hu and C. M. Li, *Chem. Commun.*, 2018, **54**, 3343–3346.

[S53] E. Demir, S. Akbayrak, A. M. Önal and S. Özkar, *ACS Appl. Mater. Interfaces*, 2018, **10**, 6299–6308.

[S54] U. Joshi, S. Malkhandi, Y. Ren, T. L. Tan, S. Y. Chiam and B. S. Yeo, *ACS Appl. Mater. Interfaces*, 2018, **10**, 6354–6360.

[S55] D. Yoon, J. Lee, B. Seo, B. Kim, H. Baik, S. H. Joo and K. Lee, *Small*, 2017, **13**, 1700052.

[S56] J. Mahmood, F. Li, S.-M. Jung, M. S. Okyay, I. Ahmad, S.-J. Kim, N. Park, H. Y. Jeong and J.-B. Baek, *Nat. Nanotechnol.*, 2017, **12**, 441–446.

[S57] P. Jiang, Y. Yang, R. Shi, G. Xia, J. Chen, J. Su and Q. Chen, *J. Mater. Chem. A*, 2017, **5**, 5475–5485.

[S58] S. Liu, Q. Liu, Y. Lv, B. Chen, Q. Zhou, L. Wang, Q. Zheng, C. Che and C. Chen, *Chem. Commun.*, 2017, **53**, 13153–13156.

[S59] S. Drouet, J. Creus, V. Collière, C. Amiens, J. García-Antón, X. Sala and K. Philippot, *Chem. Commun.*, 2017, **53**, 11713–11716.

[S60] R. Ye, Y. Liu, Z. Peng, T. Wang, A. S. Jalilov, B. I. Yakobson, S.-H. Wei and J. M. Tour, *ACS Appl. Mater. Interfaces*, 2017, **9**, 3785–3791.

[S61] Z. Pu, I. S. Amiinu, Z. Kou, W. Li and S. Mu, *Angew. Chem., Int. Ed.*, 2017, **56**, 11559–11564.

[S62] G. Sheng, J. Chen, Y. Li, H. Ye, Z. Hu, X.-Z. Fu, R. Sun, W. Huang and C.-P. Wong, *ACS Appl. Mater. Interfaces*, 2018, **10**, 22248–22256.

[S63] J. Park, H. Jin, J. Lee, A. Oh, B. Kim, J. H. Kim, H. Baik, S. H. Joo and K. Lee, *Chem. Mater.*, 2018, **30**, 6884–6892.

[S64] F. Luo, Q. Zhang, X. Yu, S. Xiao, Y. Ling, H. Hu, L. Guo, Z. Yang, L. Huang, W. Cai and H. Cheng, *Angew. Chem., Int. Ed.*, 2018, **57**, 14862–14867.

[S65] K. Yin, Y. Cheng, B. Jiang, F. Liao and M. Shao, *J. Colloid Interf. Sci.*, 2018, **522**, 242–248.

[S66] B. M. Jović, V. D. Jović, G. Branković, M. Radović and N. V. Krstajić, *Electrochim. Acta*, 2017, **224**, 571–584.

[S67] Y. Li, S. Chen, R. Long, H. Ju, Z. Wang, X. Yu, F. Gao, Z. Cai, C. Wang, Q. Xu, J. Jiang, J. Zhu, L. Song and Y. Xiong, *Nano Energy*, 2017, **34**, 306–312.

[S68] D. Bernsmeier, L. Chuenchom, B. Paul, S. Rümmler, B. Smarsly and R. Kraehnert, *ACS Catal.*, 2016, **6**, 8255–8263.

[S69] J. Li, P. Zhou, F. Li, J. Ma, Y. Liu, X. Zhang, H. Huo, J. Jin and J. Ma, *J. Power Sources*, 2016, **302**, 343–351.

[S70] K. Qi, S. Yu, Q. Wang, W. Zhang, J. Fan, W. Zheng and X. Cui, *J. Mater. Chem. A*, 2016, **4**, 4025–4031.

[S71] C. Ray, S. Dutta, Y. Negishi and T. Pal, *Chem. Commun.*, 2016, **52**, 6095–6098.

[S72] S. Kukunuri, P. M. Austeria and S. Sampath, *Chem. Commun.*, 2016, **52**, 206–209.

[S73] T. Bhowmik, M. K. Kundu and S. Barman, *ACS Catal.*, 2016, **6**, 1929–1941.

[S74] J. Chen, G. Xia, P. Jiang, Y. Yang, R. Li, R. Shi, J. Su and Q. Chen, *ACS Appl. Mater. Interfaces*, 2016, **8**, 13378–13383.

[S75] L. Jiao, F. Li, X. Li, R. Ren, J. Li, X. Zhou, J. Jin and R. Li, *Nanoscale*, 2015, **7**, 18441–18445.

[S76] Z. Zhuang, F. Wang, R. Naidu and Z. Chen, *J. Power Sources*, 2015, **291**, 132–137.

[S77] B. B. Li, S. Z. Qiao, X. R. Zheng, X. J. Yang, Z. D. Cui, S. L. Zhu, Z. Y. Li and Y. Q. Liang, *J. Power Sources*, 2015, **284**, 68–76.

[S78] J. Li, P. Zhou, F. Li, R. Ren, Y. Liu, J. Niu, J. Ma, X. Zhang, M. Tian, J. Jin and J. Ma, *J. Mater. Chem. A*, 2015, **3**, 11261–11268.

[S79] G. Darabdhara, M. A. Amin, G. A. M. Mersal, E. M. Ahmed, M. R. Das, M. B. Zakaria, V. Malgras, S. M. Alshehri, Y. Yamauchi, S. Szunerits and R. Boukherroub, *J. Mater. Chem. A*, 2015, **3**, 20254–20266.

[S80] S. Sarkar and S. Sampath, *Chem. Commun.*, 2014, **50**, 7359–7362.

[S81] Y. Feng, Y. Guan, H. Zhang, Z. Huang, J. Li, Z. Jiang, X. Gu and Y. Wang, *J. Mater. Chem. A*, 2018, **6**, 11783–11789.

[S82] C. Yang, H. Lei, W. Z. Zhou, J. R. Zeng, Q. B. Zhang, Y. X. Hua and C. Y. Xu, *J. Mater. Chem. A*, 2018, **6**, 14281–14290.

[S83] L. Lin, Z. Sun, M. Yuan, J. He, R. Long, H. Li, C. Nan, G. Sun and S. Ma, *J. Mater. Chem. A*, 2018, **6**, 8068–8077.

[S84] X. Shang, Z.-Z. Liu, S.-S. Lu, B. Dong, J.-Q. Chi, J.-F. Qin, X. Liu, Y.-M. Chai and C.-G. Liu, *ACS Appl. Mater. Interfaces*, 2018, **10**, 43561–43569.

[S85] A. Oh, H. Y. Kim, H. Baik, B. Kim, N. K. Chaudhari, S. H. Joo and K. Lee, *Adv. Mater.*, 2019, **31**, 1805546.

[S86] Y. Guan, Y. Feng, J. Wan, X. Yang, L. Fang, X. Gu, R. Liu, Z. Huang, J. Li, J. Luo, C. Li and Y. Wang, *Small*, 2018, **14**, 1800697.

[S87] H. Lv, X. Chen, D. Xu, Y. Hu, H. Zheng, S. L. Suib and B. Liu, *Appl. Catal., B*, 2018, **238**, 525–532.

[S88] J. Ge, P. Wei, G. Wu, Y. Liu, T. Yuan, Z. Li, Y. Qu, Y. Wu, H. Li, Z. Zhuang, X. Hong and Y. Li, *Angew. Chem., Int. Ed.*, 2018, **57**, 3435–3438.

[S89] K. Tang, X. Wang, Q. Li and C. Yan, *Adv. Mater.*, 2018, **30**, 1704779.

[S90] X. Xie, Y.-F. Jiang, C.-Z. Yuan, N. Jiang, S.-J. Zhao, L. Jia and A.-W. Xu, *J. Phys. Chem. C*, 2017, **121**, 24979–24986.

[S91] A. B. Soliman, M. H. Hassan, T. N. Huan, A. A. Abugable, W. A. Elmehalmey, S. G. Karakalos, M. Tsotsalas, M. Heinle, M. Elbahri, M. Fontecave and M. H. Alkordi, *ACS Catal.*, 2017, **7**, 7847–7854.

[S92] A. Mahmood, H. Lin, N. Xie and X. Wang, *Chem. Mater.*, 2017, **29**, 6329–6335.

[S93] S. Lin, Y. Liu, Z. Hu, W. Lu, C. H. Mak, L. Zeng, J. Zhao, Y. Li, F. Yan, Y. H. Tsang, X. Zhang and S. P. Lau, *Nano Energy*, 2017, **42**, 26–33.

[S94] J. Ying, G. Jiang, Z. P. Cano, L. Han, X.-Y. Yang and Z. Chen, *Nano Energy*, 2017, **40**, 88–94.

[S95] B. Jiang, F. Liao, Y. Sun, Y. Cheng and M. Shao, *Nanoscale*, 2017, **9**, 10138–10144.

[S96] G. Liu, Y. Qiu, Z. Wang, J. Zhang, X. Chen, M. Dai, D. Jia, Y. Zhou, Z. Li and P. A. Hu, *ACS Appl. Mater. Interfaces*, 2017, **9**, 37750–37759.

[S97] T. Chao, X. Luo, W. Chen, B. Jiang, J. Ge, Y. Lin, G. Wu, X. Wang, Y. Hu, Z. Zhuang, Y. Wu, X. Hong and Y. Li, *Angew. Chem., Int. Ed.*, 2017, **56**, 16047–16051.

[S98] B. Jiang, Z. Tang, F. Liao, H. Lin, S. Lu, Y. Li and M. Shao, *J. Mater. Chem. A*, 2017, **5**, 21903–21908.

[S99] X. Y. Xu, X. F. Dong, Z. J. Bao, R. Wang, J. G. Hu and H. B. Zeng, *J. Mater. Chem. A*, 2017, **5**, 22654–22661.

[S100] H. Zhang, W. Ren, C. Guan and C. Cheng, *J. Mater. Chem. A*, 2017, **5**, 22004–22011.

[S101] X.-X. Lin, A.-J. Wang, K.-M. Fang, J. Yuan and J.-J. Feng, *ACS Sustainable Chem. Eng.*, 2017, **5**, 8675–8683.

[S102] G.-R. Xu, J. Bai, L. Yao, Q. Xue, J.-X. Jiang, J.-H. Zeng, Y. Chen and J.-M. Lee, *ACS Catal.*, 2017, **7**, 452–458.

[S103] C. Wang, F. Hu, H. Yang, Y. Zhang, H. Lu and Q. Wang, *Nano Res.* 2017, **10**, 238–246.

[S104] N. Cheng, S. Stambula, D. Wang, M. N. Banis, J. Liu, A. Riese, B. Xiao, R. Li, T.-K. Sham, L.-M. Liu, G. A. Botton and X. Sun, *Nat. Commun.*, 2016, **7**, 13638.

[S105] Y. Liu, S. Liu, Z. Che, S. Zhao, X. Sheng, M. Han and J. Bao, *J. Mater. Chem. A*, 2016, **4**, 16690–16697.

[S106] T. Ding, Z. Wang, L. Zhang, C. Wang, Y. Sun and Q. Yang, *J. Mater. Chem. A*, 2016, **4**, 15309–15315.

[S107] S. Bai, C. Wang, M. Deng, M. Gong, Y. Bai, J. Jiang and Y. Xiong, *Angew. Chem., Int. Ed.*, 2014, **53**, 12120–12124.

[S108] M. Wu, P. K. Shen, Z. Wei, S. Song and M. Nie, *J. Power Sources*, 2007, **166**, 310–316.
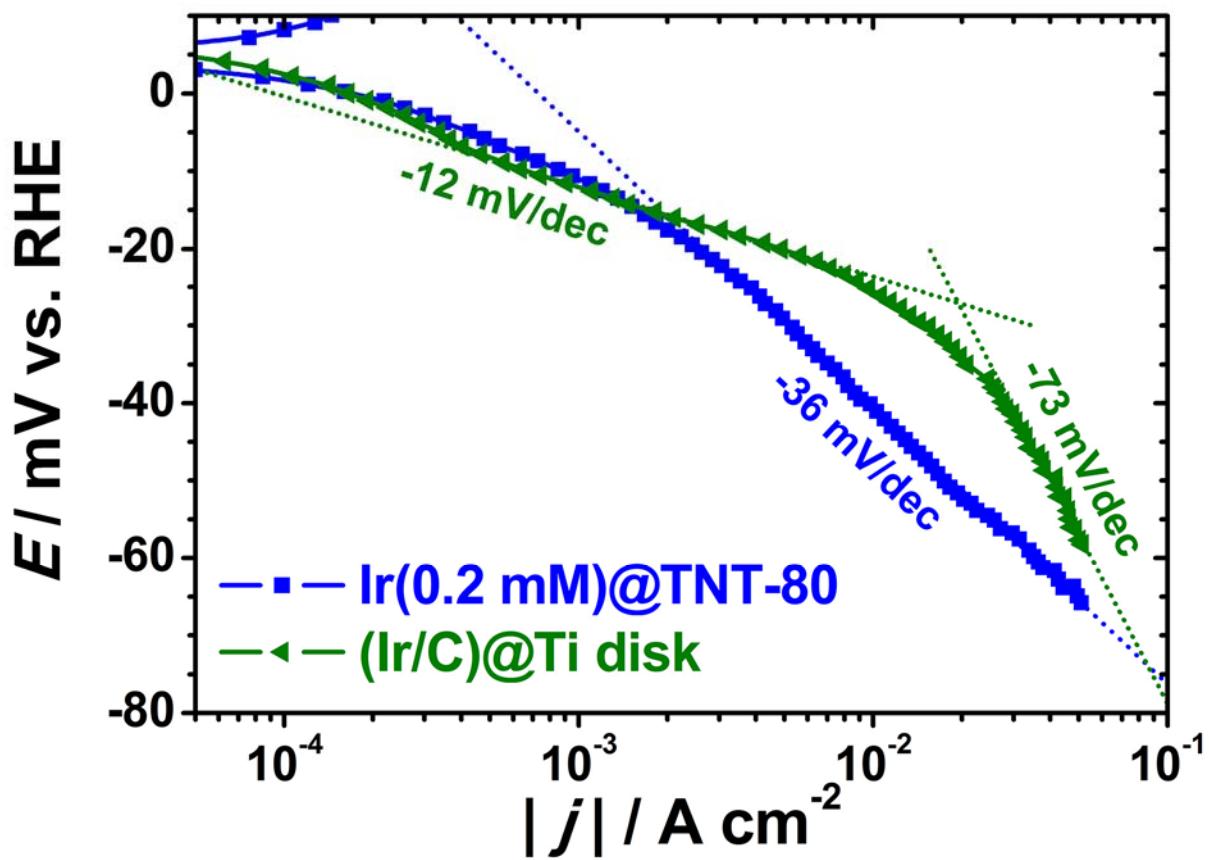
Fig. S19. Tafel plots of **Ir(0.2 mM)@TNT-80** and **(Ir/C)@Ti disk** possessing the same Ir loading of 5.7 μg_{Ir} cm^{-2}.
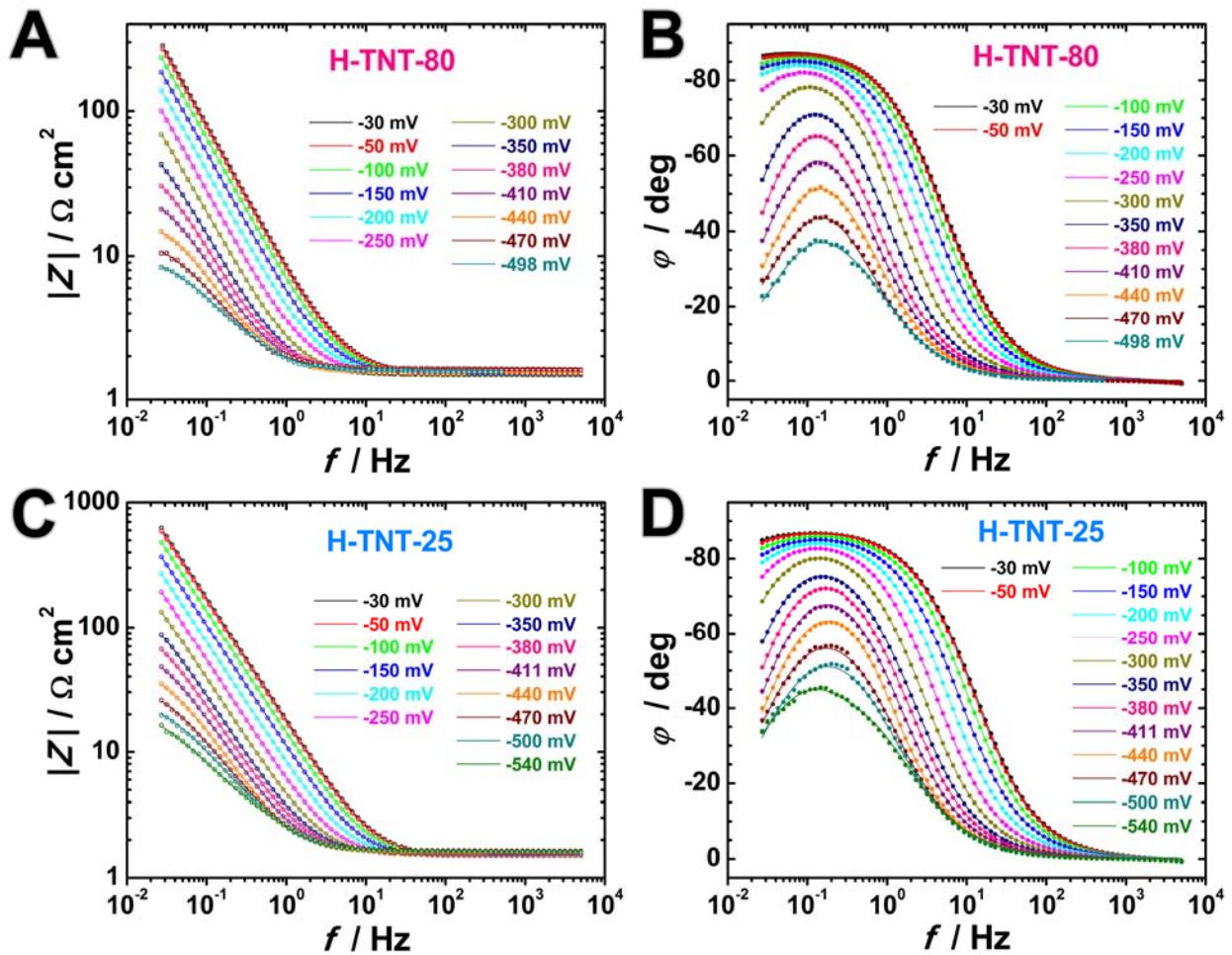
Fig. S20. Frequency dependence of impedance magnitude |*Z*| (A and C) and phase angle *φ* (B and D) at various HER overpotentials (marked in the figures) for: (A and B) **H-TNT-80** and (C and D) **H-TNT-25**. Experimental data are presented with symbols and modeled curves with solid lines.
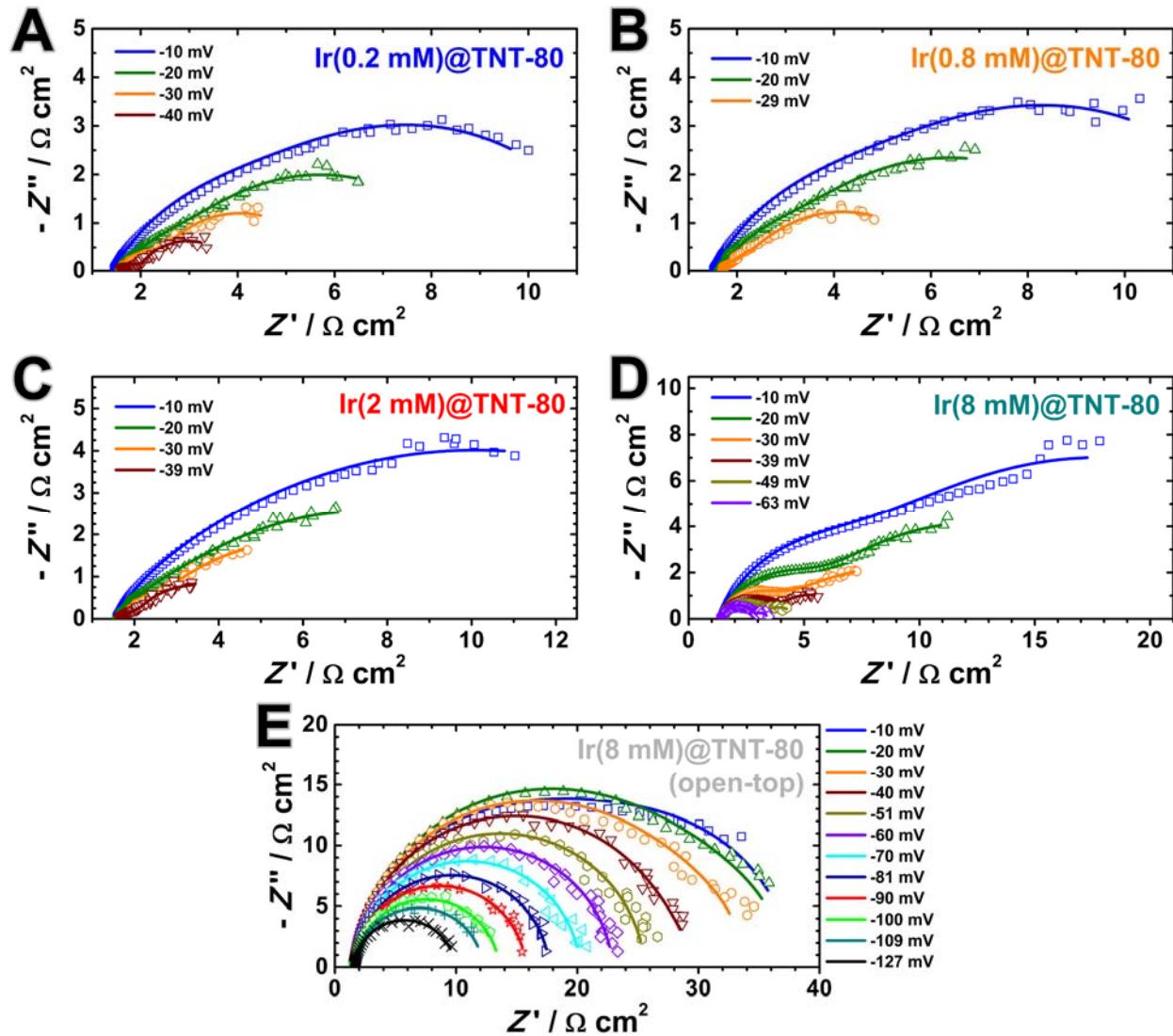
Fig. S21. Nyquist plots recorded at various HER overpotentials (marked in the figures) for: (A) **Ir(0.2 mM)@TNT-80**, (B) **Ir(0.8 mM)@TNT-80**, (C) **Ir(2 mM)@TNT-80**, (D) **Ir(8 mM)@TNT-80** and (E) **Ir(8 mM)@TNT-80 (open-top)**. Experimental data are presented with symbols and modeled curves with solid lines.
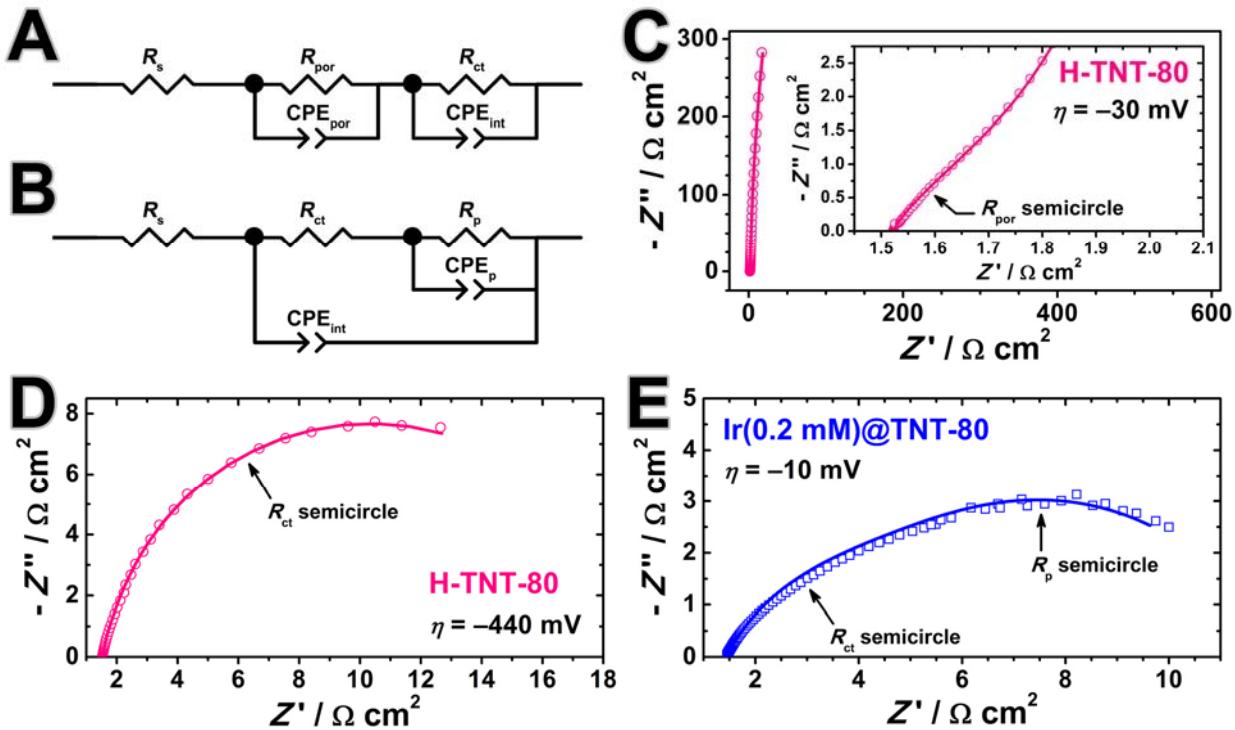
Fig. S22. Equivalent circuits applied for fitting the impedance spectra of (A) H-TNT and (B) Ir@TNT samples. Representative Nyquist plots recorded on **H-TNT-80** at overpotentials of (C) −30 mV and (D) −440 mV, and (E) on **Ir(0.2 mM)@TNT-80** at −10 mV. Experimental data are presented with symbols and modeled curves with solid lines.

Supplementary Note 3:

Due to surface inhomogeneities, TNT-based electrodes exhibit non-ideal capacitive behavior resulting in the appearance of depressed semicircles in their Nyquist plots. For that reason, all capacitors in the equivalent circuits applied for modeling (**Fig. S22A** and **S22B**) were replaced with constant phase elements (CPEs). The impedance of a CPE is given by the following expression:

$$Z_{CPE} = \frac{1}{Y(i \cdot \omega)^{\alpha}}$$

where Y is a capacitance parameter (units: S s$^{\alpha}$ cm^{-2}) and α is a non-dimensionless parameter that has a value between 0 and 1 and is related to the constant phase angle through $\varphi = -(90 \cdot \alpha)°$. This means that the center of the semicircle is depressed below the x-axis by an angle $(1-\alpha) \cdot 90°$. For $\alpha = 1$, it holds $\varphi = -90°$ and $Y = C$, i.e. the CPE behaves like an ideal capacitor.

Table S4. Equivalent circuit parameters obtained by fitting the impedance spectra of **H-TNT-80** and **H-TNT-25** recorded at different HER overpotentials.

E/V	R_s/Ω cm^2	R_{por}/Ω cm^2	Y_{por}/S s$^\alpha$ cm^{-2}	α_{por}	R_{ct}/Ω cm^2	Y_{int}/S s$^\alpha$ cm^{-2}	α_{int}
			H-TNT-80				
-0.030	1.522	0.4061	133.0e-3	0.8729	7.080e3	19.66e-3	0.9892
-0.050	1.517	0.3693	141.4e-3	0.8767	6.001e3	20.55e-3	0.9877
-0.100	1.511	0.3424	168.3e-3	0.8778	3.564e3	24.37e-3	0.9847
-0.150	1.509	0.3287	208.2e-3	0.8787	2.277e3	30.61e-3	0.9823
-0.200	1.508	0.3344	270.1e-3	0.8755	1.315e3	40.70e-3	0.9814
-0.250	1.516	0.3355	301.9e-3	0.9067	569.7	55.96e-3	0.9842
-0.300	1.476	0.2379	688.0e-3	0.8407	214.8	78.64e-3	0.9813
-0.350	1.503	0.3235	712.7e-3	0.8552	76.76	112.8e-3	0.9803
-0.380	1.600	0.2278	753.0e-3	0.8705	45.95	139.2e-3	0.9651
-0.410	1.575	0.1361	964.5e-3	0.9769	28.10	171.9e-3	0.9418
-0.440	1.542	0.1680	1.358	0.9982	17.29	217.8e-3	0.9238
-0.470	1.639	0.4307	3.440	1.000	11.85	277.2e-3	0.8724
-0.498	1.584	0.3238	1.096	1.000	8.396	326.8e-3	0.8689
			H-TNT-25				
-0.030	1.498	0.4204	124.7e-3	0.8001	10.09e3	9.165e-3	0.9833
-0.050	1.496	0.3698	124.8e-3	0.8167	8.685e3	9.633e-3	0.9816
-0.100	1.493	0.3353	144.8e-3	0.8232	5.424e3	11.71e-3	0.9781
-0.150	1.490	0.3299	188.0e-3	0.8133	3.194e3	15.17e-3	0.9757
-0.200	1.491	0.3576	252.3e-3	0.7979	1.785e3	20.63e-3	0.9761
-0.250	1.496	0.4440	323.2e-3	0.7812	888.1	28.75e-3	0.9790
-0.300	1.512	0.4618	386.3e-3	0.7907	407.1	40.38e-3	0.9788
-0.350	1.551	0.5552	377.9e-3	0.8221	175.6	55.92e-3	0.9740
-0.380	1.557	0.5399	478.8e-3	0.8295	111.3	67.65e-3	0.9689
-0.411	1.583	0.1905	865.3e-3	0.8525	72.17	82.35e-3	0.9441

-0.440	1.579	0.3859	15.91	0.3568	48.67	101.6e-3	0.9246
-0.470	1.643	0.2047	2.083	0.9662	36.43	124.9e-3	0.8768
-0.500	1.611	0.2414	1.689	1.000	27.49	143.7e-3	0.8484
-0.540	1.602	0.4929	513.3e-3	1.000	23.92	185.8e-3	0.8033
-0.580	1.557	0.6101	258.2e-3	0.8757	15.93	264.7e-3	0.8779

Table S5. Equivalent circuit parameters obtained by fitting the impedance spectra of various Ir@TNT-80 electrodes recorded at different HER overpotentials.

E/V	R_s/Ω cm^2	R_{ct}/Ω cm^2	Y_{int}/S s$^\alpha$ cm^{-2}	α_{int}	R_p/Ω cm^2	Y_p/S s$^\alpha$ cm^{-2}	α_p
			Ir(0.2 mM)@TNT-80				
-0.010	1.432	6.488	89.82e-3	0.6983	4.089	0.3617	0.8579
-0.020	1.539	3.491	163.0e-3	0.6075	4.104	0.3764	0.7916
-0.030	1.571	2.053	274.7e-3	0.5378	2.591	0.6958	0.9185
-0.040	1.571	0.4679	86.48e-3	0.6391	1.940	1.152	0.7230
			Ir(0.8 mM)@TNT-80				
-0.010	1.509	6.919	95.39e-3	0.7183	4.936	0.3944	0.8425
-0.020	1.616	3.934	167.7e-3	0.6553	4.570	0.4948	0.8021
-0.029	1.678	1.208	213.8e-3	0.5883	3.489	0.3645	0.7356
			Ir(2 mM)@TNT-80				
-0.010	1.577	2.958	67.52e-3	0.7599	14.39	0.1361	0.5036
-0.020	1.547	2.955	150.5e-3	0.6184	8.107	0.2806	0.5680
-0.030	1.619	2.793	341.3e-3	0.4742	5.707	0.4913	0.7223
-0.039	1.594	1.334	531.9e-3	0.3932	3.009	0.5853	0.8371
			Ir(8 mM)@TNT-80				
-0.010	1.451	8.176	29.09e-3	0.8234	19.96	0.1712	0.6715
-0.020	1.461	4.934	31.11e-3	0.8081	12.94	0.3227	0.6631
-0.030	1.457	2.466	23.78e-3	0.8541	10.32	0.4219	0.4965
-0.039	1.503	2.482	34.26e-3	0.7803	2.867	1.076	0.7317
-0.049	1.471	1.898	29.75e-3	0.8141	1.362	1.553	0.7076
-0.063	1.427	1.526	27.25e-3	0.8326	0.4903	3.158	0.8845
			Ir(8 mM)@TNT-80 (open-top)				
-0.010	1.524	28.10	18.83e-3	0.9505	8.054	0.1897	1.000

-0.020	1.605	31.79	18.77e-3	0.9435	3.784	0.6917	1.000
-0.030	1.628	29.31	18.51e-3	0.9523	2.899	0.7896	1.000
-0.040	1.602	26.64	18.80e-3	0.9560	1.089	3.324	1.000
-0.051	1.715	23.89	19.75e-3	0.9485			
-0.060	1.604	21.33	19.92e-3	0.9531			
-0.070	1.640	18.61	20.27e-3	0.9600			
-0.081	1.593	16.08	20.81e-3	0.9626			
-0.090	1.554	14.20	21.50e-3	0.9626			
-0.100	1.594	11.96	22.47e-3	0.9560			
-0.109	1.644	10.57	23.55e-3	0.9507			
-0.127	1.586	8.324	25.14e-3	0.9560			
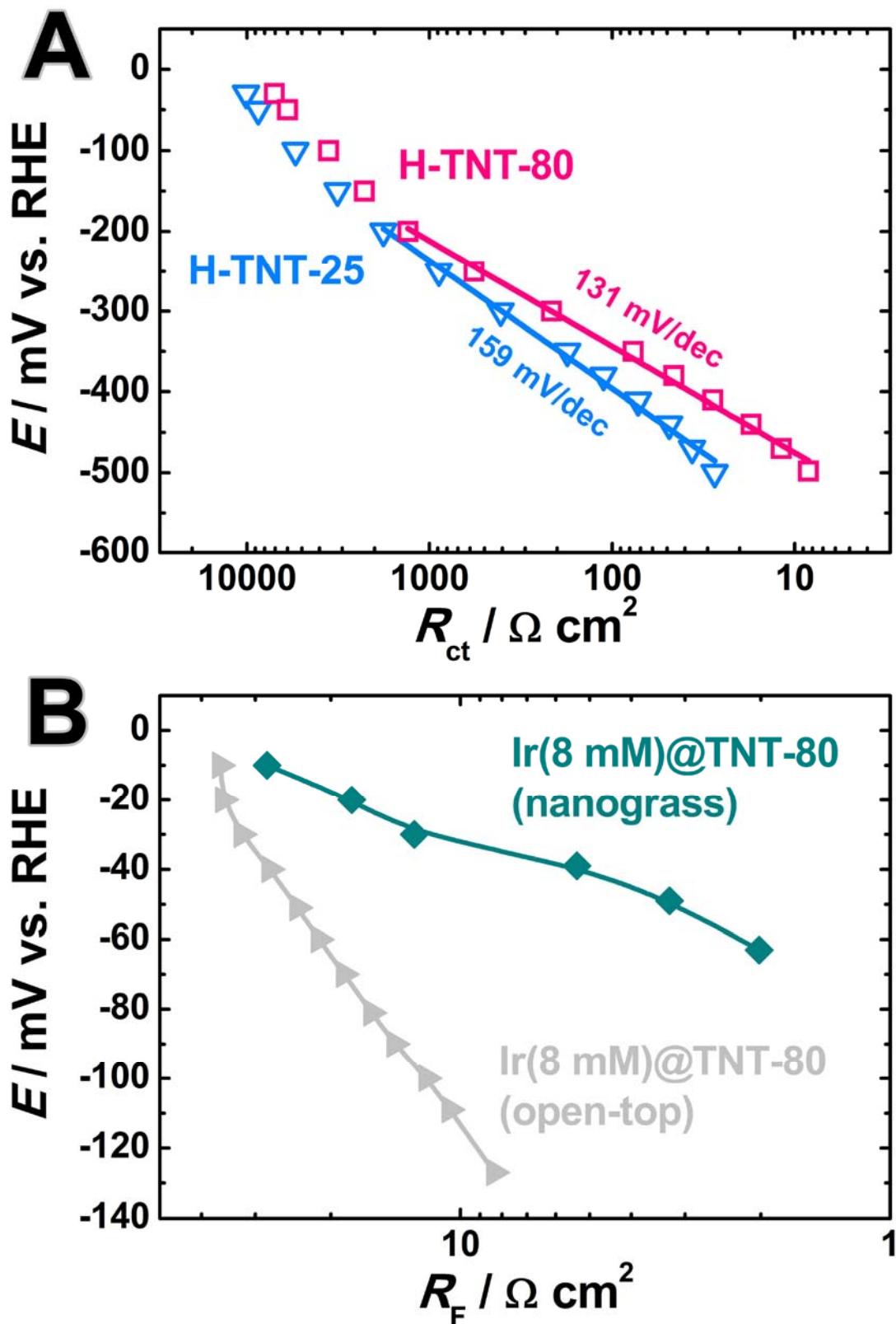
Fig. S23. *E* vs. log $(R_F)^{-1}$ plots obtained from EIS analysis for: (A) for **H-TNT-80** and **H-TNT-25** and (B) **Ir(8 mM)@TNT nanograss** and **open-top**.

Supplementary Note 4:

The average C_{int} values of the samples were estimated by means of a modified Brug equation [N4-N8]:

$$C_{int} = \left[Y_{int} \left(\frac{1}{R_s + R_{por}} + \frac{1}{R_{ct}} \right)^{\alpha_{int}-1} \right]^{\frac{1}{\alpha_{int}}}$$

where Y_{int} and α_{int} are parameters of the CPE_{int}, R_s is the solution resistance, R_{por} is the pore resistance and R_{ct} is the charge transfer resistance.

References:

[N4] G. J. Brug, A. L. G. van den Eeden, M. Sluyters-Rehbach and J. H. Sluyters, *J. Electroanal. Chem.*, 1984, **176**, 275–295.

[N5] J. Kubisztal, A. Budniok and A. Lasia, *Int. J. Hydrogen Energy*, 2007, **32**, 1211–1218.

[N6] D. Lin and A. Lasia, *J. Electroanal. Chem.*, 2017, **785**, 190–195.

[N7] U. Č. Lačnjevac, V. V. Radmilović, V. R. Radmilović and N.V. Krstajić, *Electrochim. Acta*, 2015, **168**, 178–190.

[N8] U. Č. Lačnjevac, R. Vasilić, T. Tokarski, G. Cios, P. Żabiński, N. Elezović and N. V. Krstajić, *Nano Energy*, 2018, **47**, 527–538.
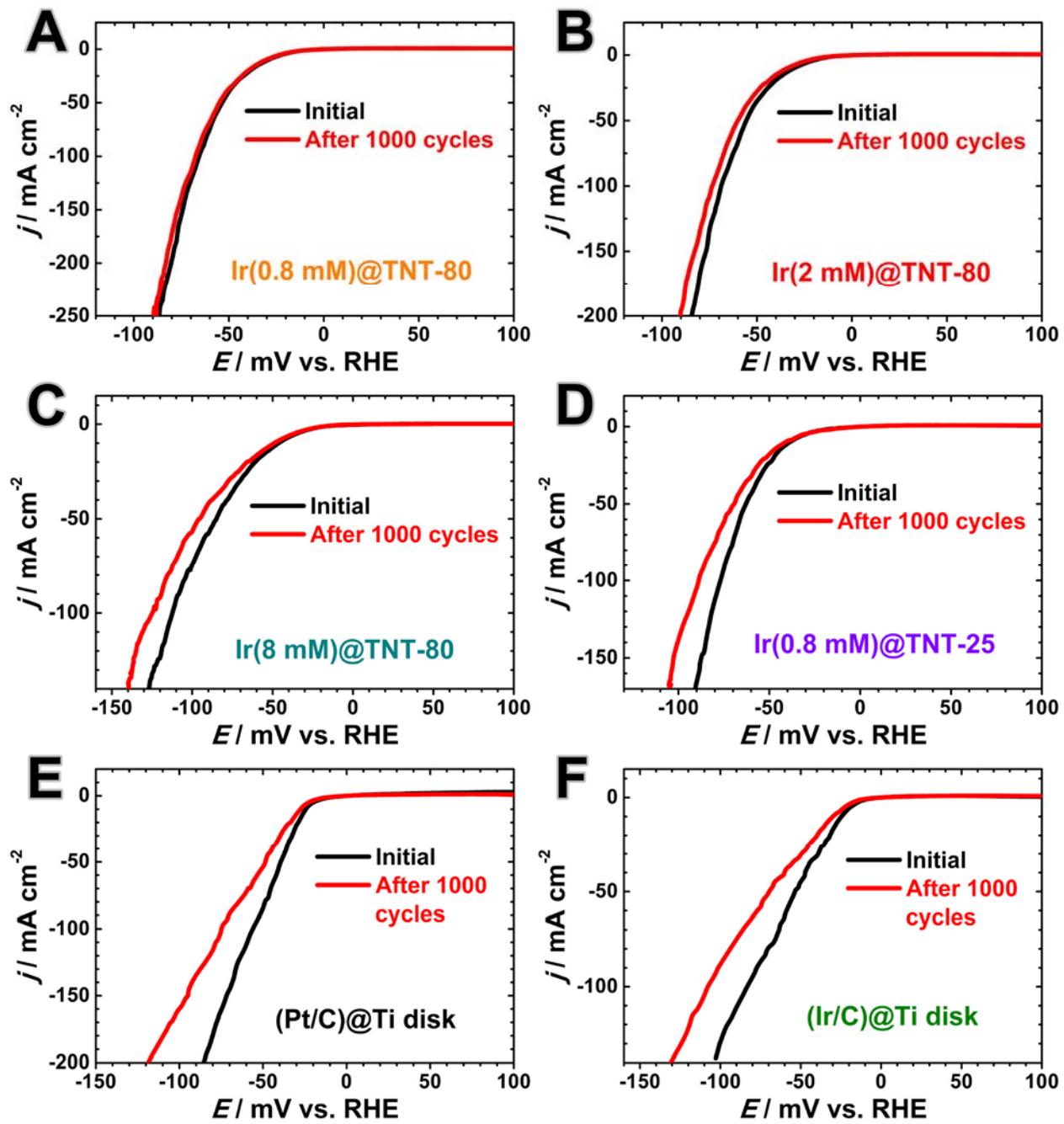
Fig. S24. Polarization curves recorded before and after applying 1000 CV scans at a sweep rate of 100 mV s^{-1} on: (A) **Ir(0.8 mM)@TNT-80**, (B) **Ir(2 mM)@TNT-80**, (C) **Ir(8 mM)@TNT-80**, (D) **Ir(0.8 mM)@TNT-25**, (E) **(Pt/C)@Ti disk** and (F) **(Ir/C)@Ti disk**. Potential cycling was performed between +0.3 V and −0.065 V for (A, B, D-F) and between +0.3 V and −0.100 V for (C).
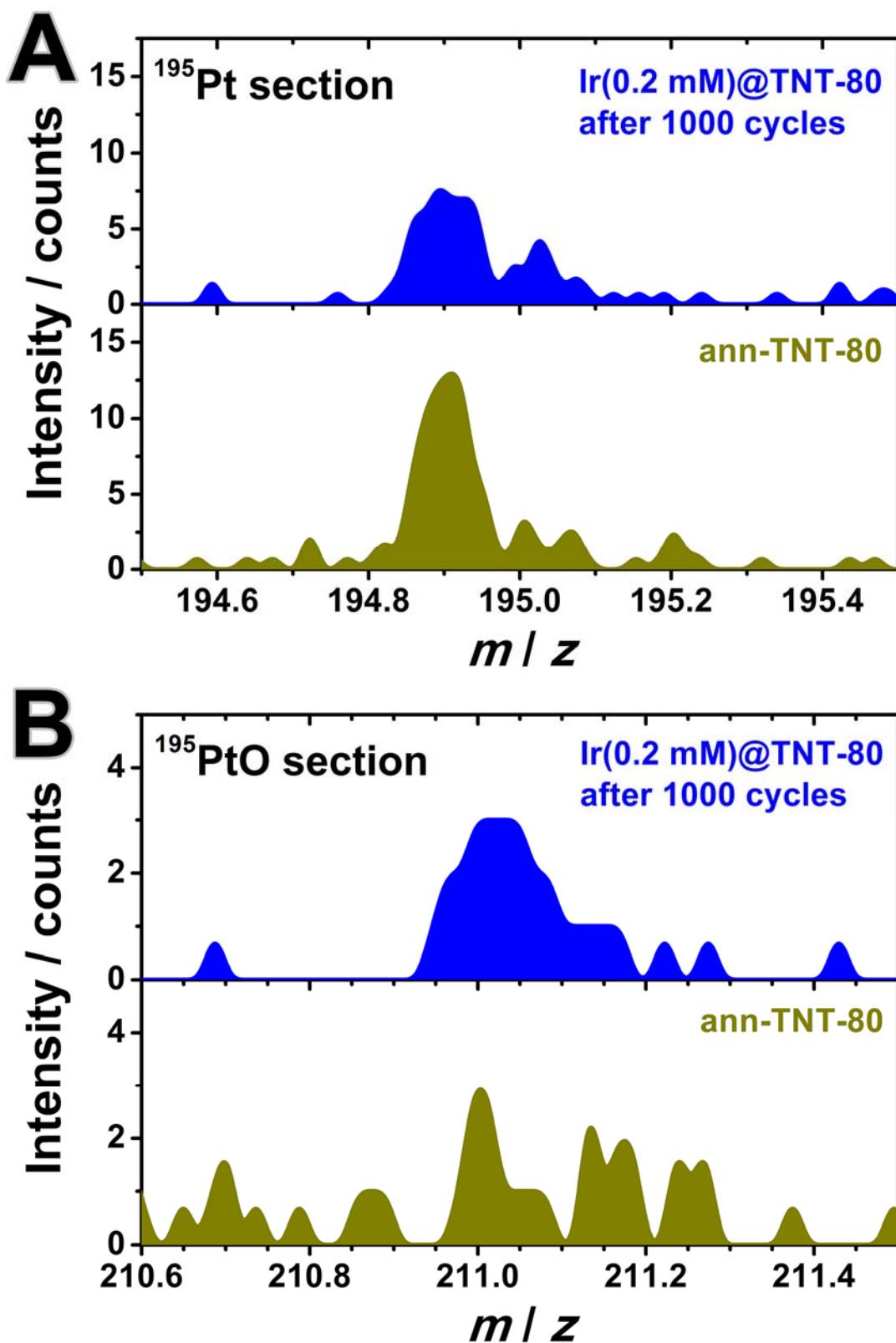
Fig. S25. ToF-SIM spectra recorded at the top surface of **Ir(0.2 mM)@TNT-80** after 1000 CV scans and **ann-TNT-80**: (A) elemental Pt and (B) PtO sections.
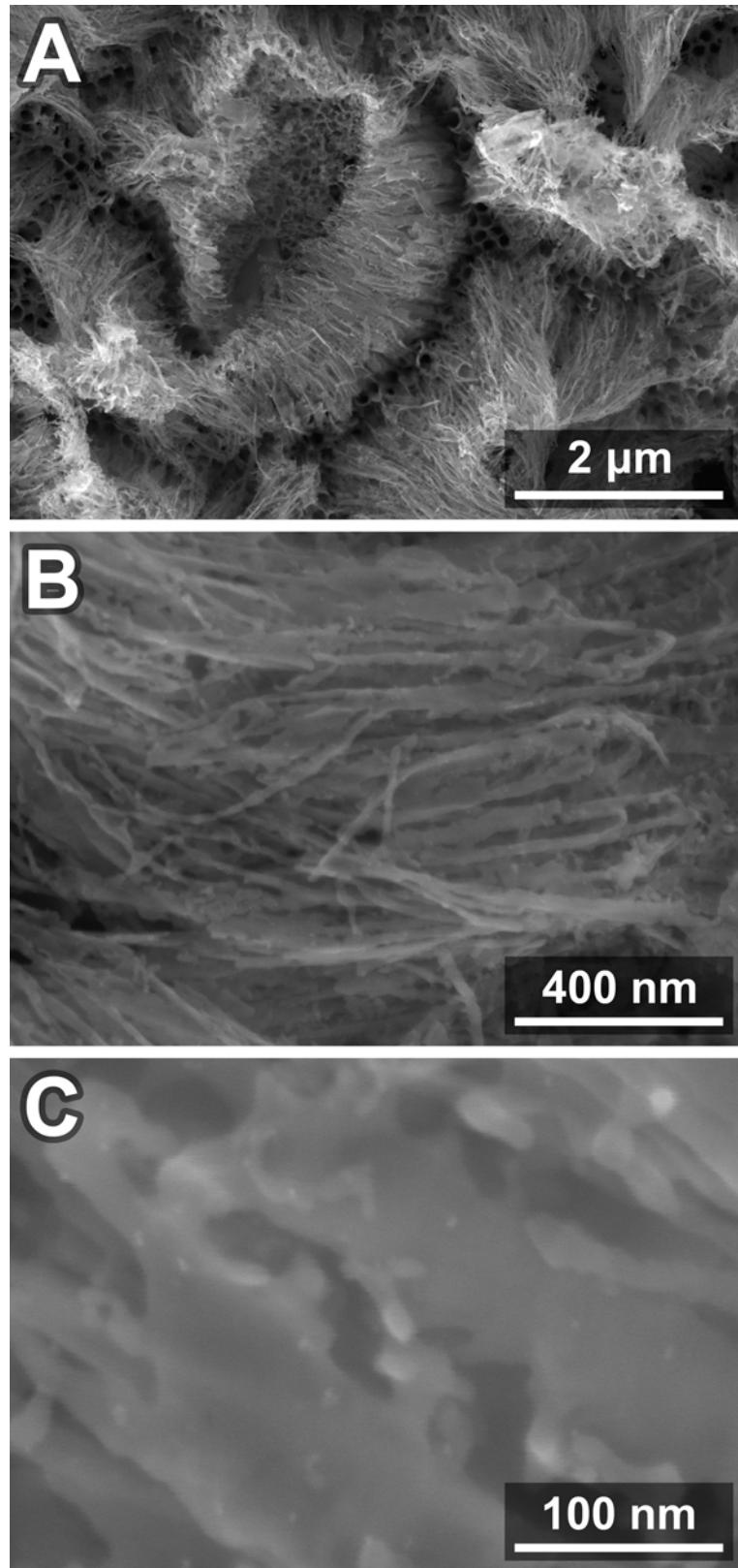
Fig. S26. FESEM images showing the top surface microstructure of **Ir(0.2 mM)@TNT-80** after the long-term chronopotentiometric stability test.
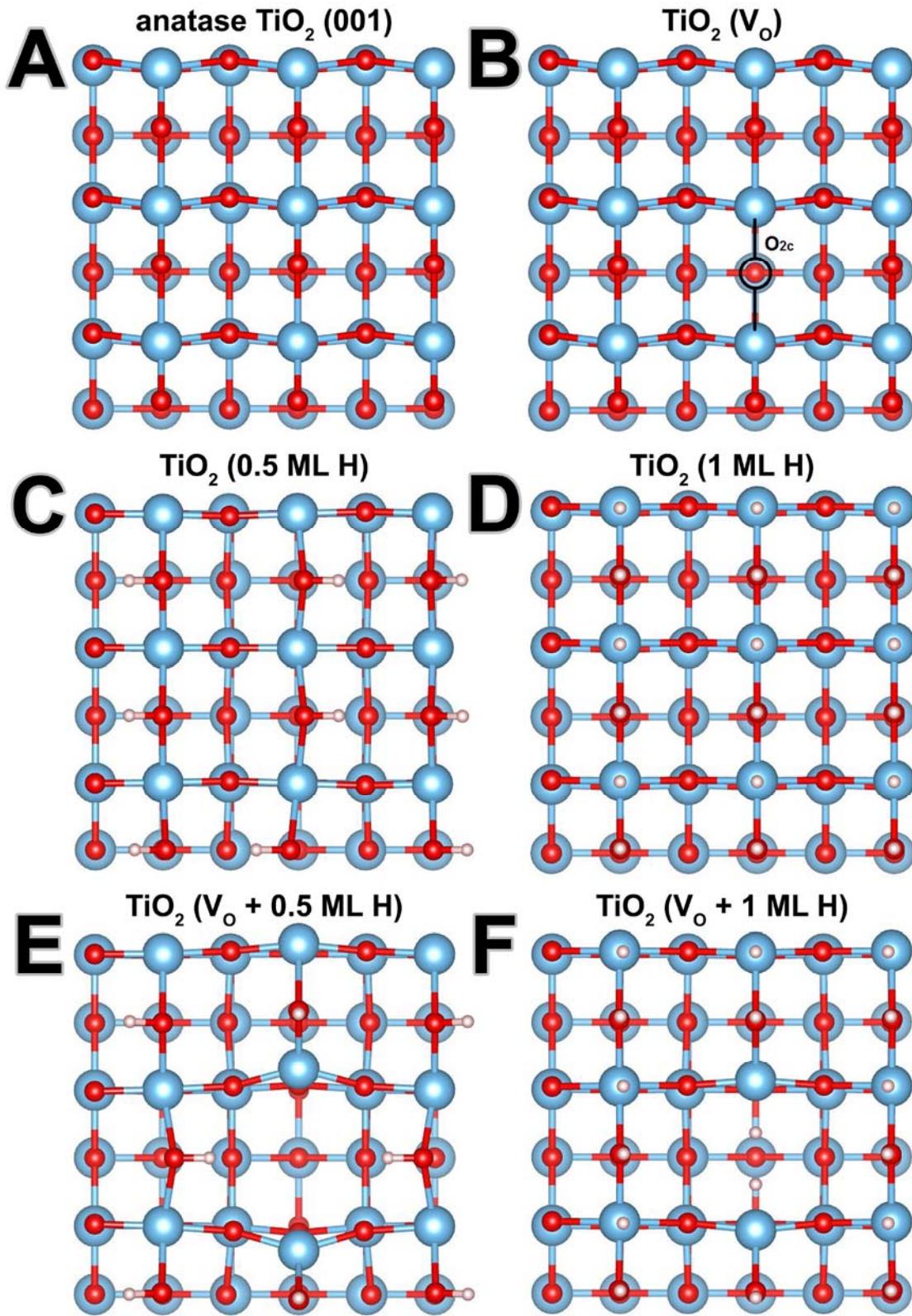
Fig. S27. Top view of different TiO$_2$ model structures considered for DFT calculations (A-F, marked in the figure). The oxygen vacancy at the bridging O$_{2c}$ site is marked in (B).
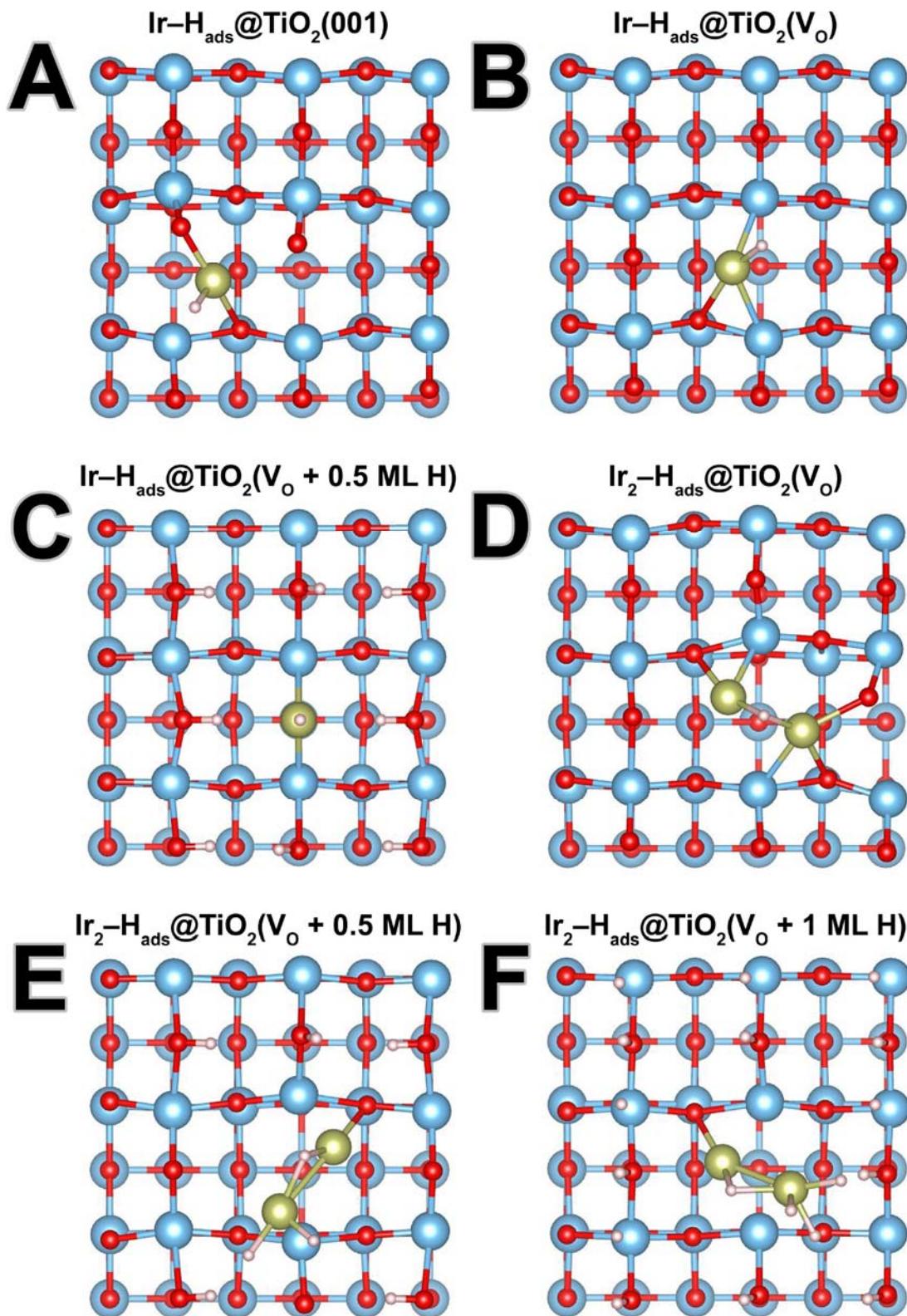
Fig. S28. DFT-simulated adsorption configurations of reaction intermediate hydrogen atoms on different Ir@TiO$_2$ model structures (A-F, marked in the figure) presented in top view.